Wide-Angle Radome Design for Low-Cost Additive Manufacturing

MATTIAS NYLANDER & MARTIN FAJERBERG
MASTER´S THESIS
DEPARTMENT OF ELECTRICAL AND INFORMATION TECHNOLOGY
FACULTY OF ENGINEERING | LTH | LUND UNIVERSITY

Wide-Angle Radome Design for Low-Cost Additive Manufacturing

Mattias Nylander
ma0810ny-s@student.lu.se
Martin Fajerberg
martin.fajerberg.393@student.lu.se

Department of Electrical and Information Technology
Lund University

Supervisor: Johan Lundgren & Sebastian Heunisch

Examiner: Daniel Sjöberg

June 2, 2022

Printed in Sweden
Tryckeriet i E-huset, Lund

Abstract

The radome, a portmanteau of the words *radar* and *dome*, is a protective dielectric cover to protect a radar from its surrounding environment. The surrounding environment can be rain, wind, sand, dust and whatever else that might harm the radar. Radomes come in many different shapes, materials and thicknesses, where each of these parameters are decided based on the need for the given radar application. The challenge is that the protective radome decreases transmission and increases reflection of the electromagnetic wave; especially for larger angles of incidence which limits the effective field-of-view.

In this project we present methods to more easily design and optimize multilayered radome structures that decrease reflections and increase transmission for a larger range of angles of incidence. Our method is to combine transmission line calculations and optimization algorithms with finite element method simulations software, where the transmission line calculations can considerably speed up and simplify an initial design. The optimization is performed for all angles of incidence of interest simultaneously, as well as the possibility to optimize for both transverse electric and transverse magnetic polarization. The design method can be used with any material and at frequencies for mmWave applications to achieve a goal of designing radomes that have reflectance below -25 dB up to 50° angles of incidence. In our thesis we found, for flat multilayer radome structures, that the transmission line calculations are very consistent with the finite element method simulations. Furthermore, measurements of prototype radomes have been performed in order to validate the simulated structures and the viability of the design procedure.

Acknowledgements

First of all we want to express our most sincere gratitude to our supervisors Johan Lundgren and Sebastian Heunisch. The uncountable hours they have used with us for guidance, feedback and long discussions have been most valuable and helped us keeping the right track and level in the thesis work. We have learned a lot about radar and radomes with our many daily discussions with Andreas Glatz, who has always been there to answer our questions. Furthermore, the help and introduction to HFSS that we got from Magnus Söderman and David Olsson has saved us from many frustrating hours spent on learning the software. We also want to thank Nenad Dordevic and Viktor Billberg for the 3D-printing of our prototype radomes. We are grateful for the many hours of discussions about radars and thesis writing that we had with Anton Almqvist and Anton Kuusela. Last but not least, we want to thank our examiner Daniel Sjöberg for the valuable help and feedback given at the final sprint of this thesis work.

Popular Science Summary

A radar utilizes electromagnetic waves to send and sense signals. Exactly in the same way as our ears, eyes and tongue are sensors and our voice and body language are transmitters to the outside world. In both the human case and the radar case, the essential sensory system needs protection from the environment around us. For example, our eyes have eyelids and our vocal cord is hidden inside our throat. Without the eyelids, our eyes would dry out and potentially be damaged from dust. In the same way, the delicate antennas, that act as receivers and transmitters of electromagnetic signals of the radar, also need protection from for example humidity, dust, wind and even birds [1]. This is where the *radome*, a combination of the words radar and dome, steps in.

The radome has the simple but very important function to protect the radar. However, the radome should be as transparent as possible to the electromagnetic waves which are received and transmitted; as well as being sufficiently robust in order to protect the radar. This is a difficult give and take balance that a radome designer needs to keep in mind; the solution in a given situation is not trivial. The development and broader usage of radars within for example surveillance and the automotive industry has increased dramatically since World War II [2]. Radars have become more mainstream and considerably cheaper as well as used for much shorter ranges. Due to this, the need for the radar to be able to "see" within wide angles has increased. Just as you will see more reflections on a window when the light hit at certain angles, the radar will also experience reflections from the radome at some angles. During this project we have developed general design methods to decrease these reflections at wide angles. Our focus has been on sandwich radomes, which is as its name implies, a radome with multiple layers of different materials. This means that, using these methods, a radome designer will be easier able to design and optimize a radome for wide angles for a given problem. What has been especially interesting is that with our suggested method, an initially, relatively simple and potentially cheap design with low reflections for a wide range of angles can be quickly calculated without the need for slow and calculation intensive simulation software.

Populärvetenskaplig Sammanfattning

En radar använder elektromagnetiska vågor för att kunna skicka och motta signaler. Precis på samma sätt som att våra öron, ögon och tungor är mottagare och vår röst och vårt kroppsspråk är sändare av signaler till världen omkring oss. För både människan och för radarn så behövs det skydd mot omgivningen. Till exempel, har våra ögon ögonlock och vår röst är dold inne i halsen. Utan ögonlock skulle ögonen torka ut och potentiellt bli skadade av dammpartiklar. På samma sätt behöver de känsliga antennerna, som fungerar som mottagare och sändare av information, också ett visst skydd från till exempel vatten, damm, vind och även fåglar [1]. Det är här *radomen*, som är en kombination av de engelska orden *radar* och *dome*, kommer in i bilden. Radomen har den enkla, men mycket viktiga, uppgiften att skydda radarn. Men radomen måste vara så transparent som möjligt för de elektromagnetiska vågorna, samtidigt som den måste vara tillräckligt robust för att skydda radarn. Detta är en svår ge och ta balans som en radomdesigner behöver ha i åtanke. Utvecklingen och de bredare användningsområden av radar, inom till exempel säkerhetsövervakning samt bilindustrin, har ökat dramatiskt sedan andra världskriget [2]. Radar har blivit vardagliga produkter, billigare och används idag för mycket kortare avstånd. Av den anledningen har behovet för att radarn kan ”se” för bredare vinklar ökat. Precis på samma sätt som att man kommer se fler reflektioner på ett fönster när ljuset träffar vid vissa vinklar, kommer en radar också uppleva reflektioner vid vissa vinklar. Under detta projekt har vi utvecklat generella designmetoder för att minska dessa reflektioner för ett brett vinkelintervall. Vårt fokus har varit på så kallade sandwich-radomer, som är precis som namnet antyder, en radom med flera lager av olika material. Detta betyder att en radomdesigner, genom att använda dessa metoder, lättare kan designa och optimera en radom for breda vinklar. Det har varit särskilt intressant att med hjälp av vår föreslagna metod kan en initial, relativt enkel och potentiellt billig design med låga reflektioner för breda vinkelintervall beräknas utan behov av långsam och beräkningsintensiv simuleringsprogramvara.

Contents

Chapter 1
Introduction

The history leading to the invention of the radar can be traced back to James Clerk Maxwell's early formulation of electromagnetic theory in the 1860's [3]. Maxwell theoretically described that electromagnetic waves can be reflected and refracted by a dielectric medium. However, it was Heinrich Hertz who in 1888 experimentally showed this concept [2], leading to the first invention and patent of an obstacle detector by Christian Hülsmeyer in 1904 [4, 5]. Since World War II, where radar was developed for military aircraft detection [2], the development of radar has increased rapidly. Today radar is widely used within a still growing range of applications such as industrial surveillance systems [6], the automotive industry [7], weather stations [8] and even gesture control [9]. However, with the emerging need for radars also comes the need for improved and versatile enclosures that protects the delicate electronics in the radar. This enclosure is called a radome. Historically the early radomes were made for aviation purposes [10, 11] of single slab materials and often in plywood [12]. However, other designs have been developed since then [13], together with the requirement of radars for a much broader range of applications. One of the most simple radome designs, is the so-called half-wavelength radome [10]. However, this design is limited in its field of view [14]. Another design, which is the core of this project, is the multilayer radome or a so called sandwich radome, which consists of multiple layers of different materials [10].

1.1 Background and Motivation to the Wide-Angle Radome

In our case, we have chosen to develop general design methods for radomes with low reflection over a wide-angle interval. We will not focus on high mechanical strength. Additionally, a wide band radome is not a goal in itself, but we will require that the radome has a bandwidth of at least 1 %. However, our requirement is to have low reflection and high transmission for a wide range of angles. In this way, the radar will experience less interference by internal reflections and is able to "see" in a broader view, both horizontally and vertically, compared to the half-wavelength radome. Also, the focus has been on flat radomes since we believe that ideally the flat-shaped radome makes the performance of a radar independent on where the antennas are located. Furthermore, the focus has been on sandwich radomes. The motivation behind this is that multilayer radomes has shown to

have better performance for wide angles compared to the single slab [15]. Also, we believe that with more layers it is easier to have some design freedom in order to fit the design for certain needs.

1.2 Scope

For this thesis, we aim to develop general and easily implementable design methods for wide-angle radomes for low-cost additive manufacturing. Using calculations in Python, finite element method simulation software like HFSS and COMSOL Multiphysics, we aim to simplify the radome design process. In this way, we want to be able to evaluate and compare different sandwich structures with the single slab structure, as well as finding methods to do this. In the end we aim to do final measurements of some of the results to validate simulations. The goal is to have a reflectance below -25 dB up to 50° angle of incidence.

1.3 Previous Work

Much work has recently been done within the field of radome design in order to increase the performance for different use cases. One of which is the publication from Qamar et al., 2020 [16] where the goal is to present a design technique for a multi-layered ultra-wide-band radome for communication systems and dual-polarized radar usage. In [16] various radome designs are introduced, such as multiple layered structures with different materials for the different layers. The goal of this work, as mentioned, was to create a radome with a wide bandwidth without changing the overall size of the radome. However, we will investigate similar structures but with a different goal in mind, that is to investigate a structure with increased wide-angle performance.

Further, in the paper by Mazlumi, 2018 [17], a design method for a multiple layered radome structure is proposed. This was done for both normal incidence to the radome as well as oblique incidence, this is of interest to us since our goal is to investigate the performance over angles of incidence. The problem with this article, as compared to our work, is that the design method is only done for one angle at a time. What we are interested in is the design over several angles simultaneously.

The main problem, from our point of view, with these previous works is that while they investigate similar radome structures the wide angle performance is not of interest. Also, they do not focus on the development of the B-sandwich design (see figure 3.2b) which we are interested in. What we can learn from these is the design methodology for radome structures and then build upon this in order to investigate a different use case.

1.4 Thesis Disposition

In **Chapter 2** we cover the theory needed for this thesis. First, we go through theory of basic electromagnetic wave propagation and the theory behind reflections of electromagnetic waves on dielectric materials together with losses in these materials. The angular dependence is also described and the differences between the linear polarization cases, namely TM and TE polarization. Next, we very briefly discuss the antenna and two-port fundamentals needed for our radome design theory. In **Chapter 3** we introduce the different radome structures used in this thesis. **Chapter 4** covers a description of the calculation, optimization and simulation methods that we have used, together with our design methodology. In **Chapter 5** we, as a pre-study, present results related to the simple half-wavelength slab radome for benchmarking. **Chapter 6** is the core of our work and here results related to the multilayer radome are presented. Both concrete results and more general design methods are investigated, especially related to the A- and B-sandwich and the honeycomb structure. **Chapter 7** covers radome measurement results as well as 3D-printed radomes that we have created. **Chapter 8** presents full 2D simulations in COMSOL Mulitphysics. In the end a discussion and conclusion can be found in **Chapter 9** and **Chapter 10** respectively.

Chapter 2
Theory

2.1 Electromagnetic Waves

When energy travels through a medium from point A to B it is often done in the form of waves, some examples being sound, light and microwaves [18]. The fundamental difference between these is that sound falls into the category of mechanical waves while visible light and microwaves are called electromagnetic (EM) waves [19]. However, while a mechanical wave requires a medium and molecules to travel, the EM waves can travel through vacuum.

Electromagnetic waves consist of two parts, an electric field and a magnetic field and can be described by periodic oscillations between these fields where they are orthogonal to each other. The radiation of electromagnetic waves occur when there is a periodic shift in the electric and magnetic fields, such as an electron moving through a conductive material [19]. The relation between the electric and magnetic field was written by Maxwell and compiled in Maxwell's equations for the time domain shown in 2.1 [20].

$$\nabla \times \boldsymbol{E} = -\frac{\partial \boldsymbol{B}}{\partial t} \tag{2.1a}$$

$$\nabla \times \boldsymbol{H} = \boldsymbol{J} + \frac{\partial \boldsymbol{D}}{\partial t} \tag{2.1b}$$

$$\nabla \cdot \boldsymbol{D} = \rho \tag{2.1c}$$

$$\nabla \cdot \boldsymbol{B} = 0 \tag{2.1d}$$

In (2.1) the quantities are as follow: $\boldsymbol{E}$ is the electric field intensity [V/m], $\boldsymbol{H}$ is the magnetic field intensity[A/m], $\boldsymbol{J}$ is the electric current density[A/m^2], $\boldsymbol{D}$ is the electric flux density[C/m^2], $\boldsymbol{B}$ is the magnetic flux density [T] and ρ is the volume charge density [C/m^3] [20]. Furthermore ∇ is defined as

$$\nabla = \hat{\boldsymbol{x}}\frac{\partial}{\partial x} + \hat{\boldsymbol{y}}\frac{\partial}{\partial y} + \hat{\boldsymbol{z}}\frac{\partial}{\partial z} \tag{2.2}$$

where $\hat{\boldsymbol{x}}$, $\hat{\boldsymbol{y}}$ and $\hat{\boldsymbol{z}}$, are the unit vectors in the x, y and z directions.

If we assume an isotropic material then [14, Ch. 1]

$$\boldsymbol{D} = \epsilon \boldsymbol{E} \tag{2.3a}$$

$$\boldsymbol{B} = \mu \boldsymbol{H} \tag{2.3b}$$

where μ is the permeability and ϵ is the permittivity of the medium in which the wave propagates. If we further assume a source free region, $\boldsymbol{J} = \boldsymbol{0}$ and $\rho = 0$, and that the electromagnetic wave is travelling in an isotropic, linear and homogeneous material as well as assuming that both the electric field $\boldsymbol{E}$ and magnetic field $\boldsymbol{H}$ has a harmonic time dependence $e^{\mathrm{j}\omega t}$, we can rewrite the Maxwell equations (2.1) to [14, Ch. 1]

$$\nabla \times \boldsymbol{E} = -\mathrm{j}\omega\mu \boldsymbol{H} \tag{2.4a}$$

$$\nabla \times \boldsymbol{H} = \mathrm{j}\omega\epsilon \boldsymbol{E} \tag{2.4b}$$

$$\epsilon \nabla \cdot \boldsymbol{E} = 0 \tag{2.4c}$$

$$\mu \nabla \cdot \boldsymbol{H} = 0 \tag{2.4d}$$

The permeability is defined as [14, Ch. 1]

$$\mu = \mu_0 \mu_\mathrm{r} = \mu_0 (1 + \chi_\mathrm{m}) \tag{2.5}$$

where μ_0 is the permeability in vacuum, μ_r is the relative permeability and χ_m is the magnetic susceptibility. Throughout this thesis we only consider materials with no magnetic properties, i.e. $\chi_\mathrm{m} = 0$ and thus $\mu = \mu_0$. The permittivity ϵ of a medium, which we throughout this thesis refer to as the *dielectric constant*, is defined as [14, Ch. 1]

$$\epsilon = \epsilon_0 \epsilon_\mathrm{r} = \epsilon_0 (1 + \chi) \tag{2.6}$$

where ϵ_0 is the dielectric constant in vacuum, ϵ_r is the relative dielectric constant of the medium or material in which the wave propagates and χ is the electric susceptibility. The speed of light in a medium is given by [14, Ch. 1]

$$v = \frac{1}{\sqrt{\mu\epsilon}} \tag{2.7}$$

and the speed of light in vacuum is

$$c = \frac{1}{\sqrt{\mu_0 \epsilon_0}} \tag{2.8}$$

Furthermore, we can define the wavelength λ

$$\lambda = \frac{v}{f} \tag{2.9}$$

The wavelength in vacuum then becomes $\lambda_0 = c/f$. From here we see that the wavelength is dependent, not only on the frequency, but also on which medium the wave is propagating in. The wavenumber k is defined as

$$k = \frac{2\pi}{\lambda} = \omega\sqrt{\mu\epsilon} \tag{2.10}$$

from where the wavenumber in vacuum is $k_0 = 2\pi/\lambda_0$.

Taking the curl of both left hand and right hand side of (2.4a) and (2.4b) we get if constant material parameter are assumed

$$\nabla \times (\nabla \times \boldsymbol{E}) = \mu\epsilon\omega^2\boldsymbol{E} \tag{2.11a}$$

$$\nabla \times (\nabla \times \boldsymbol{H}) = \mu\epsilon\omega^2\boldsymbol{H} \tag{2.11b}$$

For a vector $\boldsymbol{A}$ then $\nabla \times (\nabla \times \boldsymbol{A}) = \nabla(\nabla \cdot \boldsymbol{A}) - \nabla^2\boldsymbol{A}$. Utilizing this together with the relations in (2.4c), (2.4d) and (2.10), we can finally rewrite (2.11), which gives us our time harmonic relations as

$$\nabla^2\boldsymbol{E} = -k^2\boldsymbol{E} \tag{2.12a}$$

$$\nabla^2\boldsymbol{H} = -k^2\boldsymbol{H} \tag{2.12b}$$

where k is the wavenumber as defined in (2.10). For a plane wave propagating in the z direction, (2.12) is solved by the ansatz $e^{-\mathrm{j}kz}$ [10], which gives the solution to the electric field $\boldsymbol{E}$ of a wave propagating in the z direction as [10]

$$\boldsymbol{E} = \boldsymbol{E}_0 e^{-\mathrm{j}kz} \tag{2.13}$$

This is a convenient solution to the wave equation that we use in the next section.

2.2 Losses in Dielectric Materials

Whenever a wave is propagating through a lossy dielectric material in a certain direction z it is both attenuated and phase shifted [10]. The dielectric constant as stated in (2.6) of a material is in general a complex number and can be written as [10]

$$\epsilon = \epsilon' - \mathrm{j}\epsilon'' \tag{2.14}$$

where ϵ' is the real part and ϵ'' is the imaginary part of the dielectric constant. The relative loss of electric energy is then defined as the loss tangent $\tan\delta$

$$\tan\delta = \frac{\epsilon''}{\epsilon'} \tag{2.15}$$

such that

$$\epsilon = \epsilon'(1 - \mathrm{j}\tan\delta) \tag{2.16}$$

The plane wave in the z-direction (2.13) through the dielectric takes the form [10]

$$\boldsymbol{E} = \boldsymbol{E}_0 e^{-\mathrm{j}kz} = \boldsymbol{E_0} e^{-(\alpha+\mathrm{j}\beta)z} = \boldsymbol{E_0} e^{-\gamma} \tag{2.17}$$

where z is the direction of propagation, $k = 2\pi/\lambda$ is the wavenumber, α is the attenuation constant and β is the phase constant, with

$$\alpha = \omega\sqrt{\frac{\mu\epsilon'}{2}(\sqrt{1 + (\tan\delta)^2} - 1)} \tag{2.18}$$

and

$$\beta = \omega\sqrt{\frac{\mu\epsilon'}{2}(\sqrt{1 + (\tan\delta)^2} + 1)} \tag{2.19}$$

where ω is the angular frequency. Ideally, we do not want any loss of energy in our material. From here it is possible to see that it is desired to keep the loss tangent as small as possible. Also, we can define the loss coefficient as $\gamma = \alpha + \mathrm{j}\beta$. In general, a dielectric material with a thickness d is lossy and the absorption loss of energy will be proportional to $e^{-\gamma d}$ as can be seen from (2.17) [21].

2.3 TE & TM Polarization

In this thesis we only consider linearly polarized waves. For a linearly polarized EM wave we can have Transverse Electric (TE) polarized and Transverse Magnetic (TM) polarized wave propagating onto the radome surface [14, Ch. 7]. An illustration of TE and TM polarization is shown in figure 2.1. For TE polarization (figure 2.1a), the electric field is perpendicular to the plane of incidence and for TM polarization (figure 2.1b) the electric field is parallel to the plane of incidence [19]. The electric field and the magnetic field are perpendicular to each other as shown in figure 2.1.

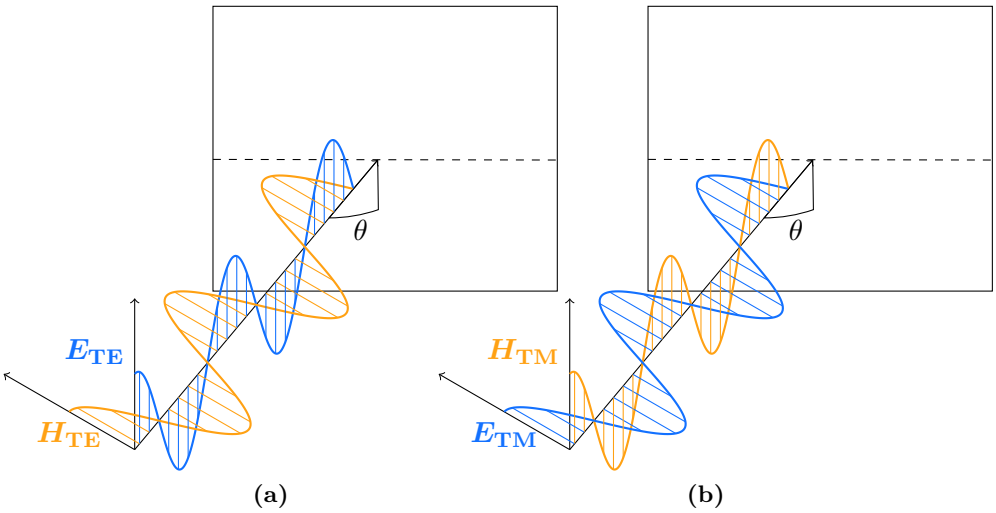

Figure 2.1: Illustration of TE & TM polarization onto the radome at a given angle of incidence θ with TE mode.(a) shows the TE polarization mode and (b) shows the TM polarization mode.

2.4 Reflections

A much more serious problem than losses when designing radomes is reflections [22]. When an electromagnetic wave is propagating from one medium (for example air) to another medium (for example a dielectric material), then a part of the wave will be reflected at the interface between the two media [14, Ch. 5]. Ideally, we want a radome where no reflection occurs at the interface between radome and air. If we approximate the permittivity of air to that of vacuum, then the relative dielectric constant of air can be written as $\epsilon_{\mathrm{r,air}} = 1$. With this the air can be assumed to be an ideal dielectric where the wave impedance Z is real valued and is given by [14, Ch. 2]

$$Z = \sqrt{\frac{\mu}{\epsilon}} \tag{2.20}$$

Which gives, for the case of air, $Z_{\mathrm{air}} \approx 377\ \Omega$. This means that for an arbitrary dielectric (with no magnetic properties, *i.e.* $\mu = \mu_0$) we get

$$Z_{\mathrm{diel}} = \sqrt{\frac{\mu_0}{\epsilon_0 \epsilon_r}} \approx \frac{377}{\sqrt{\epsilon_r}}\Omega \tag{2.21}$$

where Z_{diel} is the impedance of the dielectric. For a radome it is desired to have minimum reflections at the interface between radome and air which is obtained in the most simple way if $Z_{\mathrm{air}} = Z_{\mathrm{diel}}$. From (2.20) and (2.21) we clearly see that it is desired to have a dielectric constant $\epsilon_r \approx 1$. However, this is not possible in reality and we have to consider other techniques to achieve minimum reflection.

2.4.1 The Single Dielectric Slab with Air on Both Sides

The simplest radome can be seen as a single dielectric slab with thickness d, see figure 2.2. At the first boundary between air and the slab ($z = 0$) we will get a loss from left to right due only to the boundary which can be expressed as the reflection coefficient $\rho(z)$ [21]

$$\rho(0) = \frac{E_-(0)}{E_+(0)} = \frac{Z_{\text{diel}} - Z_{\text{air}}}{Z_{\text{diel}} + Z_{\text{air}}} \tag{2.22}$$

where E_- is the reflected electric field and E_+ is the transmitted electric field at the boundary. At the second boundary ($z = d$), going from dielectric to air, we will get the elementary reflection coefficient

$$\rho(d) = \frac{Z_{\text{air}} - Z_{\text{diel}}}{Z_{\text{air}} + Z_{\text{diel}}} = -\rho(0) \tag{2.23}$$

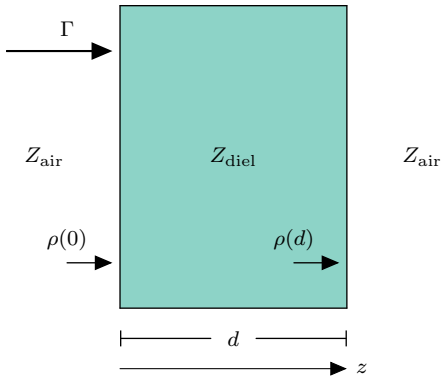

Figure 2.2: Single dielectric slab with air on either side.

However, we are interested in the total reflection Γ at the interface between air and slab due to reflections at both boundaries. In the case when we have air on either side of the slab we get [14, Ch. 5]

$$\Gamma = \frac{\rho(0)(1 - e^{-2\mathrm{j}kd})}{1 - \rho^2(0)e^{-2\mathrm{j}kd}} \tag{2.24}$$

where k is the wavenumber in the dielectric slab. From (2.24) we see that we can cancel the total reflection ($\Gamma = 0$) if $e^{-2\mathrm{j}kd} = 1$. Or to express this in another way

$$d = n\frac{\lambda}{2} = n\frac{\lambda_0}{2\sqrt{\epsilon_{\text{r,diel}}}}, \quad n \in \mathbb{Z} \tag{2.25}$$

where $\lambda = \lambda_0/\sqrt{\epsilon_{\text{r,diel}}}$ is the wavelength in the dielectric and λ_0 is the wavelength in free space. If we consider the lossless case then a hand-waving but more intuitive way to see this is that since the dielectric is $\lambda/2$ thick then the transmitted wave at the first boundary travels 180° to the second boundary and is then reflected back from the second boundary, where it is phase shifted −180° and travels another

180° back to the first boundary where it then cancels out the reflection, so that zero net wave is reflected [22].

2.4.2 The Single Dielectric Slab - General Case

When we do not have air on both sides of the slab, but for example air on one side and another, infinitely long, dielectric on the other side, then the situation is a bit different. The impedance on the left side of the slab Z_1 is then not equal to the impedance on the right side of the slab Z_2. This case is shown in figure 2.3.

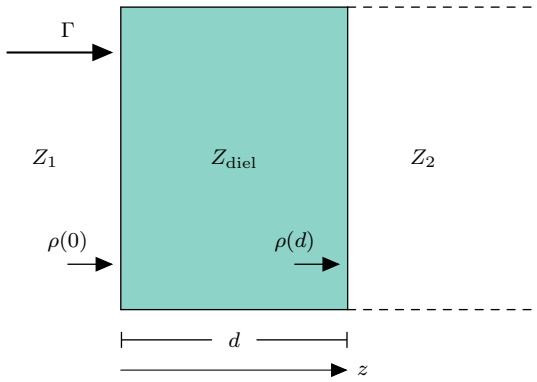

Figure 2.3: Single dielectric slab with with different media on either side.

This means that $\rho(0) \neq -\rho(d)$ and then equation 2.24 can be re-written into equation 2.26 [14, Ch. 5]

$$\Gamma = \frac{\rho(0) + \rho(d)e^{-2\mathrm{j}kd}}{1 + \rho(0)\rho(d)e^{-2\mathrm{j}kd}} \tag{2.26}$$

from which Γ is zero only if $e^{2\mathrm{j}kd} = -1$ and $\rho(0) = \rho(d)$. The fact that we will have zero reflection if $\rho(0) = \rho(d)$, *i.e.*

$$\frac{Z_{\text{diel}} - Z_1}{Z_{\text{diel}} + Z_1} = \frac{Z_2 - Z_{\text{diel}}}{Z_2 + Z_{\text{diel}}} \tag{2.27}$$

gives finally $\Gamma = 0$ if (2.28) is fulfilled [14, Ch. 5]

$$Z_{\text{diel}} = \sqrt{Z_1 Z_2} \text{ and } d = (2n+1)\frac{\lambda}{4} \quad n \in \mathbb{Z} \tag{2.28}$$

Using 2.21 we can see that if $Z_1 = 377\ \Omega$ (impedance of air) then the condition $Z_{\text{diel}} = \sqrt{Z_1 Z_2}$ is equivalent to that $\epsilon_{\text{r,diel}} = \sqrt{\epsilon_{\text{r},2}}$.

2.4.3 Reflections at oblique incidence

So far, we have only covered reflections for the normal incidence, *i.e.* the angle of incidence $\theta = 0°$. However, at oblique incidence, when $0° < \theta \leq 90°$, the reflections

on the radome will behave differently than at $\theta = 0°$. At oblique incidence to the radome, the polarization dependent wave impedance will be [14, Ch. 7]

$$Z_{\mathrm{p},m} = \begin{cases} Z_m \cos\theta_m, & \text{TM Polarization} \\ \dfrac{Z_m}{\cos\theta_m}, & \text{TE Polarization} \end{cases} \tag{2.29}$$

where p denotes the polarization (either TM or TE polarization) and $m = 0, 1, 2, \ldots$ denotes the medium at which the wave propagates. We can then utilize (2.21) to rewrite (2.29) related to the polarization dependent relative dielectric constant ϵ_m.

$$\sqrt{\epsilon_{\mathrm{p},m}} = \begin{cases} \dfrac{\sqrt{\epsilon_m}}{\cos\theta_m}, & \text{TM Polarization} \\ \sqrt{\epsilon_m}\cos\theta_m, & \text{TE Polarization} \end{cases} \tag{2.30}$$

Whenever a plane wave is travelling from one medium with an impedance to another medium with another impedance, then the angle of refraction will change according to Snell's law as can be seen in figure 2.4, where $\epsilon_{\mathrm{r},0} < \epsilon_{\mathrm{r},1} < \epsilon_{\mathrm{r},2}$.

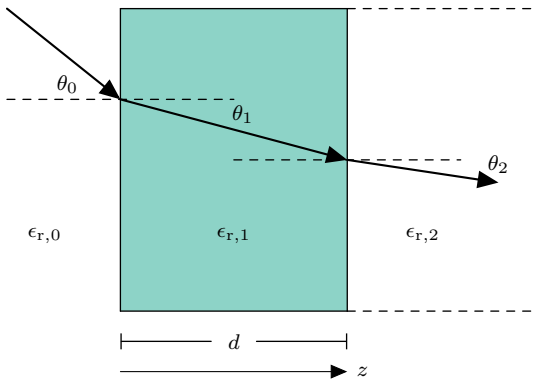

Figure 2.4: A plane wave changing propagation direction when going from one medium to another. In this figure $\epsilon_{\mathrm{r},0} < \epsilon_{\mathrm{r},1} < \epsilon_{\mathrm{r},2}$.

Snell's law yields [14, Ch. 7]

$$\sqrt{\epsilon_{m+1}}\sin\theta_{m+1} = \sqrt{\epsilon_m}\sin\theta_m \tag{2.31}$$

Using trigonometric formulas and Snell's law we can identify that for the angle $\theta_{\mathrm{m+1}}$ we have

$$\cos\theta_{m+1} = \sqrt{1 - \frac{\epsilon_m}{\epsilon_{m+1}}\sin^2\theta_m} \tag{2.32}$$

And identifying that, in a multilayer structure as in figure 2.4, (2.32) gives the relation between any layer with index m and the first incidence angle θ_0 as

$$\cos\theta_m = \sqrt{1 - \frac{\epsilon_0}{\epsilon_m}\sin^2\theta_0} \tag{2.33}$$

Combining (2.30) and (2.32) we can rewrite the elementary reflection between two dielectric materials as

$$\rho_{\mathrm{TM}} = \frac{\sqrt{\frac{\epsilon_{m+1}}{\epsilon_m} - \sin^2\theta_m} - \frac{\epsilon_{m+1}}{\epsilon_m}\cos\theta_m}{\sqrt{\frac{\epsilon_{m+1}}{\epsilon_m} - \sin^2\theta_m} + \frac{\epsilon_{m+1}}{\epsilon_m}\cos\theta_m} \tag{2.34}$$

for the TM polarization case. For the TE polarization case we get

$$\rho_{\mathrm{TE}} = \frac{\cos\theta_m - \sqrt{\frac{\epsilon_{m+1}}{\epsilon_m} - \sin^2\theta_m}}{\cos\theta_m + \sqrt{\frac{\epsilon_{m+1}}{\epsilon_{m+1}} - \sin^2\theta_m}} \tag{2.35}$$

From (2.34) it can be identified that there is an angle θ_{B} that has $\rho_{\mathrm{TM}} = 0$ for the TM polarized case. This angle is called the Brewster angle and is described as [14, Ch. 7]

$$\tan\theta_{\mathrm{B}} = \sqrt{\frac{\epsilon_{m+1}}{\epsilon_m}} \tag{2.36}$$

Using the relation in (2.33) we can identify for θ_1 and θ_2 in figure 2.4 that

$$\cos\theta_1 = \sqrt{1 - \frac{\epsilon_0}{\epsilon_{\mathrm{r},1}}\sin^2\theta_0}, \quad \cos\theta_2 = \sqrt{1 - \frac{\epsilon_0}{\epsilon_{\mathrm{r},2}}\sin^2\theta_0} \tag{2.37}$$

using (2.37) and (2.30) we can retrieve the reflections $\rho(0,\theta_0)$ and $\rho(d,\theta_0)$ dependent on the angle of incidence θ_0 at each interface in figure 2.4 in terms of dielectric constants using (2.21) for the two polarization cases as

$$\rho(0,\theta_0)_{\mathrm{TM}} = \frac{\sqrt{\frac{\epsilon_{\mathrm{r},1}}{\epsilon_{\mathrm{r},0}} - \sin^2\theta_0} - \frac{\epsilon_{\mathrm{r},1}}{\epsilon_{\mathrm{r},0}}\cos\theta_0}{\sqrt{\frac{\epsilon_{\mathrm{r},1}}{\epsilon_{\mathrm{r},0}} - \sin^2\theta_0} + \frac{\epsilon_{\mathrm{r},1}}{\epsilon_{\mathrm{r},0}}\cos\theta_0} \tag{2.38}$$

$$\rho(d,\theta_0)_{\mathrm{TM}} = \frac{\sqrt{\frac{\epsilon_{\mathrm{r},2}}{\epsilon_{\mathrm{r},1}} - \sin^2\theta_0} - \frac{\epsilon_{\mathrm{r},2}}{\epsilon_{\mathrm{r},1}}\cos\theta_0}{\sqrt{\frac{\epsilon_{\mathrm{r},2}}{\epsilon_{\mathrm{r},1}} - \sin^2\theta_0} + \frac{\epsilon_{\mathrm{r},2}}{\epsilon_{\mathrm{r},1}}\cos\theta_0} \tag{2.39}$$

$$\rho(0,\theta_0)_{\mathrm{TE}} = \frac{\cos\theta_0 - \sqrt{\frac{\epsilon_{\mathrm{r},1}}{\epsilon_{\mathrm{r},0}} - \sin^2\theta_0}}{\cos\theta_0 + \sqrt{\frac{\epsilon_{\mathrm{r},1}}{\epsilon_{\mathrm{r},0}} - \sin^2\theta_0}} \tag{2.40}$$

$$\rho(d,\theta_0)_{\mathrm{TE}} = \frac{\cos\theta_0 - \sqrt{\frac{\epsilon_{\mathrm{r},2}}{\epsilon_{\mathrm{r},1}} - \sin^2\theta_0}}{\cos\theta_0 + \sqrt{\frac{\epsilon_{\mathrm{r},2}}{\epsilon_{\mathrm{r},1}} - \sin^2\theta_0}} \tag{2.41}$$

The previous analysis means that we can transform the general case single dielectric slab to oblique incidence angle as well. In order to get zero reflection Γ for the case in figure 2.4 we can now change the condition in (2.27) into

$$\rho(0,\theta_0)_{\mathrm{TM}} = \rho(d,\theta_d)_{\mathrm{TM}} \quad \text{TE Polarization} \tag{2.42}$$

$$\rho(0,\theta_0)_{\mathrm{TE}} = \rho(d,\theta_d)_{\mathrm{TE}} \quad \text{TM Polarization} \tag{2.43}$$

We can see from the relations (2.42) and (2.43) with help from (2.38), (2.39), (2.40) and (2.41) that they are true and angle independent in the case when

$$\epsilon_{\mathrm{r},1} = \sqrt{\epsilon_{\mathrm{r},0}\epsilon_{\mathrm{r},2}} \tag{2.44}$$

which is exactly the same as the condition for the dielectric constants for normal incidence angle. However, the thickness d of the slab with dielectric constant $\epsilon_{\mathrm{r},1}$ changes to [10]

$$d = (2n+1)\frac{\lambda_0}{4\sqrt{\epsilon_{\mathrm{r},1} - \sin^2\theta_0}}, \quad n \in \mathbb{Z} \tag{2.45}$$

This now shows that the radome thickness for the zero reflection case is dependent on the angle of incidence.

2.5 Antenna Fundamentals

2.5.1 Antenna Radiation

For this thesis, we consider radome design for frequencies in the range between 20-60 GHz. We are in the Fresnel zone [20, 23] if

$$0.62\sqrt{\frac{D^3}{\lambda}} \leq r \leq \frac{2D^2}{\lambda} \tag{2.46}$$

where D is the largest dimension of the antenna. Throughout this thesis we assume that the radome is in the Fresnel zone.

2.5.2 Gain and Directivity

The directivity is given by the maximum value of the directivity function $D(\theta,\psi)$, where θ and ψ are spherical coordinates [20], which gives the power in a specific direction in relation to the power from a theoretical isotropic antenna which has uniform radiation in all directions. For example, if the directivity of a certain antenna $D = 2$ (corresponding to a magnitude of 3 dBi), then it means that the antenna has a maximum power which is twice that of the power of an isotropic counterpart in the same direction. The directivity is usually measured in decibel and denoted dBi. With the directivity we can see that if the directivity for an antenna increases this means that the antenna has a more focused and directed signal. At the same time we can define the gain parameter G for an antenna, which compared to the directivity D, is the directivity of power taking losses due to mismatch into account. This means that $G < D$ and we can define the radiation efficiency η in equation (2.47) [20].

$$\eta \equiv \frac{G}{D} \tag{2.47}$$

What we can see here is that since the relation between the gain and the directivity is given by the antenna efficiency η this is a constant factor which is angular independent.

2.5.3 S-Parameters

The scattering parameters (S-parameters) describe the relation in input and output of power of waves between electrical ports [24].

A schematic of a two-port is shown in figure 2.5, where we have one port (Port 1) on the left side and a another port (Port 2) on the right side.

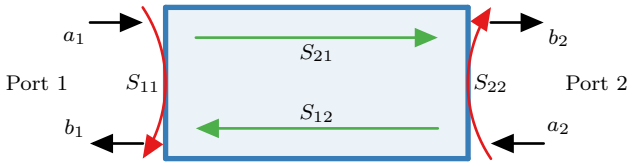

Figure 2.5: A schematic of a two port with scattering parameters S_{11}, S_{21}, S_{12} and S_{22} as well as incident waves a_1, a_2 and reflected waves b_1, b_2.

From Port 1 we have an incident wave a_1 and a reflected wave b_1 and from Port 2 we have an incident wave a_2 and a reflected wave b_2. We can then see the S-parameters S_{11} and S_{22} as a measure of reflected power from Port 1 and Port 2 respectively and see S_{21} and S_{12} as a measure of transmitted power for Port 1 and Port 2 respectively [24]. For this thesis, we assume that the radomes are reciprocal and symmetric, which means that $S_{11} = S_{22}$ and $S_{21} = S_{12}$ [25]. Although non-reciprocal radomes have been shown to be possible [26, 27], we only consider designs for symmetric and reciprocal radomes. Thus we consider S_{11} as a measure of reflection and S_{21} as a measure of transmission on our radome. S-parameters are complex valued and S_{11} and S_{21} are defined as [24]

$$S_{11} = \left.\frac{b_1}{a_1}\right|_{a_2=0} \tag{2.48a}$$

$$S_{21} = \left.\frac{b_2}{a_1}\right|_{a_2=0} \tag{2.48b}$$

We can then define the reflected power as

$$\text{Reflected Power} = 20 \cdot \log|S_{11}| \quad [\text{dB}] \tag{2.49}$$

and the transmitted power as

$$\text{Transmitted Power} = 20 \cdot \log|S_{21}| \quad [\text{dB}] \tag{2.50}$$

The relations in (2.49) and (2.50) are used in order to measure the performance of the radome designs in terms of reflection and transmission.

2.6 Boresight Error

The boresight error is determined as the difference in the mechanical and optical axis of the antenna. The bore-sight error (BSE) is introduced when either the antenna radiation is not aligned with the mechanical axis or when the radome affects the radiation. Since the wave has a longer travel path at higher angles the discrepancy between the electrical and mechanical axis can increase giving angular errors. This is important to minimize since angular distortions can affect how the antenna perceives object and give false information on where the object is located [22, 28].

Chapter 3
Radomes

As mentioned earlier, the main objective with this thesis is to present a radome design method. In this chapter the radome designs that we focus on will be presented and described further in detail.

The dielectric material is a very important factor since this determines how well the transmitted wave can pass through the radome. Ideally, for a simple single-slab radome, we want a minimal difference of the dielectric constant between the surrounding air and the radome. For air the relative permittivity is approximately 1 and most polymers used for radomes have an ϵ_r value of about 2 to 6 for a specific frequency range [29]. In order to have a radome material that is close to the ϵ_r of air we would need to use materials, such as Styrofoam, that are in general softer and has a lower mechanical robustness. When choosing a material there will be a trade-off between the electrical optimization and the mechanical demands.

3.1 The Half-Wavelength Radome and its Challenges

The simplest method to design a radome with theoretically zero reflection is to aim for a radome with a half wavelength thickness and air on both sides. However, the problem is that theoretically zero reflection is only true for normal incidence to the radome, if a flat radome as shown in figure 3.1 is assumed.

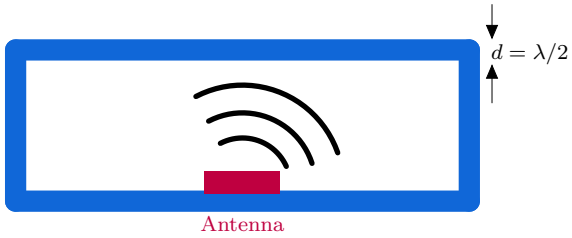

Figure 3.1: Simple schematic of a rectangular radome with a half wavelength thickness and a single antenna in the center.

The reason is that waves propagating at angles away from the boresight angle will have a longer travel distance through the radome and therefore experience more reflection at higher angles [22]. For optimal transmission, if angles away from the normal incidence is to be taken into consideration, then we need to modify (2.25) [10]

$$d = n\frac{\lambda_0}{2\sqrt{\epsilon_r - \sin^2\theta}} \tag{3.1}$$

where $0^\circ \leq \theta \leq 90^\circ$ is the angle of incidence of the plane wave. We see that if $\theta = 0^\circ$ (normal incidence) then this equation simplifies to (2.25).

A solution to satisfy (3.1) could be to make the radome successively thicker at higher angles. Another solution is to make a perfect half-sphere radome, with a half wavelength thickness, which means that the wave will travel a half wavelength regardless of angle [22]. In both of these cases we assume that the antenna is placed in the center. However, in most cases there are multiple antennas, a so called antenna array [9, 22, 30], which means that the antennas will not be placed in the center. Another consideration with half-wavelength radomes is that they are narrow banded and the band narrows even more with increasing multiples of half wavelengths thickness [10] (*i.e.* $n > 1$ in equation 2.25). On the other hand, making the radome thicker will also make it more durable.

3.2 Variations in Radome Design

There are other approaches than the half-wavelength design that can be implemented in order to design a radome with high transmission, which we have investigated throughout this thesis. There are different techniques such as sandwich designs, frequency selective surface structures or meta-material implementations. With these methods it is possible to utilize other structural changes than the thickness in order to increase the overall performance of the radome.

Meta-materials are one of the design solutions to minimize the reflections introduced by the radome. A meta-material is a non-natural material often in the form of a dielectric material with periodic structures embedded [31, 32]. One use of metamaterials is to create a honeycomb structure [33] [34] which has an effective dielectric constant given by the Maxwell-Garnett approximation (3.4) [35].

The third option for designing a radome is to use what is called a sandwich structure which consists of multiple layers. There are different types of sandwich structures called A, B, C and multi-layered which can be seen in figure 3.2.

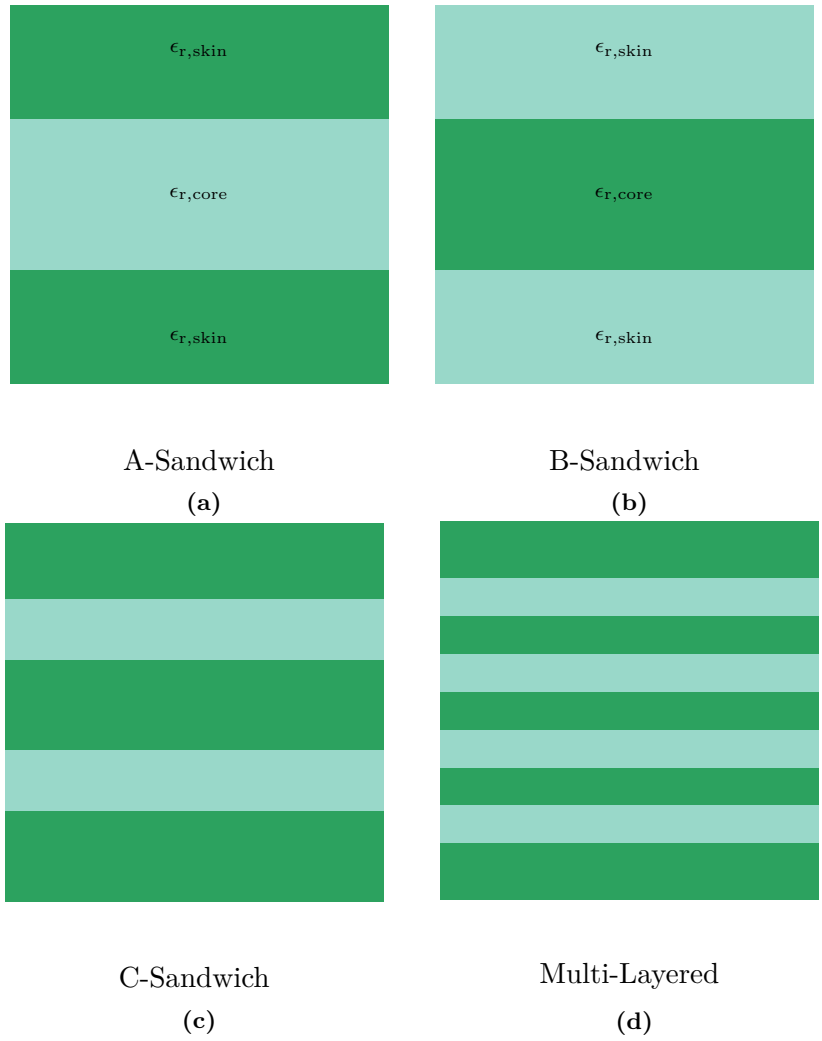

Figure 3.2: Various designs of the sandwich radome with layers with different dielectric constants.

With an A-Sandwich design, seen in figure 3.2a, better strength to weight ratio can be achieved by using a lighter material with low relative dielectric constant as the inner layer, hereby referred to as the core material. This design has seen wide usage within the aerospace industry as a preferable strength to weight ratio can be achieved [36]. What we also see is that with a sandwich design such as the A-type we have a core with low $\epsilon_{r,core}$ which minimizes losses since it is close to that for air and often a thin high dielectric skin is used in order to protect the softer core material. Even though the dielectric constant is usually quite large in order to have a robust material, the skin will act as a thin-wall radome and with a thickness of around $\lambda/10$ or less the losses and reflections will be very small [10]. In the case of the half wavelength radome it is possible to calculate the optimal

thickness at which we get zero reflection Γ at normal incidence for the sandwich design. If the dielectric constants of the core and skin of the A-Sandwich together with a predetermined thickness of the skin is known, it is possible to calculate the optimum thickness of the core at a certain operating frequency that will give theoretically zero reflection at a certain angle θ. In order to calculate the optimal thickness of the core for an A-sandwich design we can look at (3.2) as suggested in [17]

$$e^{2\mathrm{j}\delta_2} = \frac{(\rho_{0,1} + e^{2\mathrm{j}\delta_1}\rho_{1,2})(1 + e^{2\mathrm{j}\delta_1}\rho_{0,1}\rho_{1,2})}{(\rho_{0,1} + e^{-2\mathrm{j}\delta_1}\rho_{1,2})(1 + e^{-2\mathrm{j}\delta_1}\rho_{0,1}\rho_{1,2})} \tag{3.2}$$

where

$$\delta_i = k_0 d_i \sqrt{\epsilon_\mathrm{r} - \sin^2(\theta)}, \quad i = 1, 2 \tag{3.3}$$

and $k_0 = 2\pi/\lambda_0$ is the free space wavenumber, d_i is the thickness of layer i and layer 2 is the core layer. $\rho_{0,1}$ is the elementary reflection between air and the skin layer 1 as defined in (2.22) and $\rho_{1,2}$ is the reflection between skin layer and core layer. First we solve δ_2 from (3.2). Then we can use δ_2 in order to solve the optimal thickness of the core, d_2, from (3.3) [17].

In figure 3.2b we see an illustration of the B-Sandwich design. The B-Sandwich can be considered as an inverted A-sandwich, *i.e.* that the skin has a lower dielectric constant than the core. With the B-Sandwich, we do not necessarily need a thin skin and we have more freedom in the choice of core thickness [37]. With a B-Sandwich we also have the possibility to utilize (2.28) in order minimize reflections, this since the skin has a lower dielectric constant than the core. (2.28) is then fulfilled if the relative dielectric constants have the relationship $\epsilon_{\mathrm{r,skin}} = \sqrt{\epsilon_{\mathrm{r,core}}}$ and the thickness of the skin is $d_{\mathrm{skin}} = (2n+1)\lambda/4$.

The C-Sandwich seen in figure 3.2c consists of five layers and is two A-Sandwiches stacked on each other. The advantage of the C-Sandwich compared to the single A-Sandwich is that it will have zero reflection at both the frequency at which each isolated A-Sandwich has zero reflection, as well as at the frequency at which the reflection from each A-Sandwich has opposite phase which gives maximal destructive interference [37].

At last we define the multi-layered sandwich design seen in figure 3.2d. This design can be an arbitrary number of layers with many different dielectric constants in any order. For example it can be a stack of more than two A-Sandwiches or a stack of B-Sandwiches.

3.3 Honeycomb Core

An alternative method of creating an A-sandwich structure with a low dielectric core material is to create a structure that is partially filled with air instead of using a softer low dielectric material. One of the more common ways of solving

this within e.g aerospace engineering [36] and RF engineering [38] is the use of honeycomb structures as a core. With a honeycomb structure it is possible to either use a separate honeycomb material as the core or construct the sandwich radome in such a way that the whole structure consists of the same material but the layers of the lower dielectric constant material of the sandwich being partly filled with air. With the latter case we have a lot more freedom when designing our prototype since the effective dielectric constant of the honeycomb can be approximated with the Maxwell-Garnett mixing formula. The Maxwell-Garnett mixing formula, with only one inclusion, is given by [35]

$$\epsilon_{\text{eff}} = \epsilon_{\text{m}} \frac{2\delta(\epsilon_{\text{i}} - \epsilon_{\text{m}}) + \epsilon_{\text{i}} + 2\epsilon_{\text{m}}}{2\epsilon_{\text{m}} + \epsilon_{\text{i}} - \delta(\epsilon_{\text{i}} - \epsilon_{\text{m}})} \tag{3.4}$$

In (3.4) the effective dielectric constant of the structure ϵ_{eff} is calculated from the dielectric constants of the inclusion ϵ_{i}, the medium ϵ_{m} and the filling factor δ. If we know the effective dielectric constant for a certain A-Sandwich design, we can then calculate δ from (3.4).
In the case of the honeycomb design, the air ϵ_{air}, would correspond to ϵ_{m} and the dielectric material to fill with ϵ_{diel}, would correspond to ϵ_{i}. The filling factor is the volume fraction of the inclusion material compared to that of the medium. A honeycomb can be constructed from hexagons. An illustration of a hexagon is shown in figure 3.3, where we see the dimensions a, b and t_{wall}, where a is the length of the side, $b = a\sqrt{3}/2$ and t_{wall} is the thickness of the wall. The orange wall is the dielectric material and the white area inside is air.

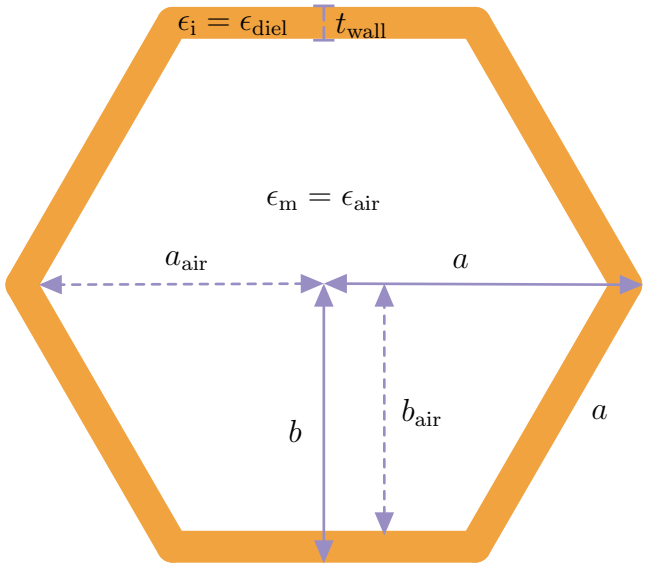

Figure 3.3: Honeycomb structure with a solid wall, a and b indicate the sizes in the x, y direction. The length in x direction a is equal to that of the length of the side.

The area A of the entire hexagon is calculated as

$$A = \frac{3\sqrt{3}}{2}a^2 \tag{3.5}$$

The inner hexagon which is the area filled with air has a side a_{air} and $b_{\text{air}} = a_{\text{air}}\sqrt{3}/2$ which means that the area filled with air A_{air} is

$$A_{\text{air}} = \frac{3\sqrt{3}}{2}a_{\text{air}}^2 \tag{3.6}$$

The dielectric material area (orange in figure 3.3) is then

$$A_{\text{diel}} = A - A_{\text{air}} \tag{3.7}$$

Since the height (direction into the paper) is the same for both the air filled honeycomb and the outer honeycomb then the filling factor δ is given by

$$\delta = \frac{A_{\text{diel}}}{A} = 1 - \frac{a_{\text{air}}^2}{a^2} \tag{3.8}$$

Assuming that we know the filling factor equated from (3.4), and have decided a side of the honeycomb a then we can calculate the side of the inner honeycomb a_{air} as

$$a_{\text{air}} = a\sqrt{1-\delta} \tag{3.9}$$

Finally the thickness of the wall t_{wall} is given by

$$t_{\text{wall}} = b - b_{\text{air}} = \frac{\sqrt{3}}{2}(a - a_{\text{air}}) = \frac{\sqrt{3}}{2}a(1 - \sqrt{1-\delta}) \tag{3.10}$$

This means that, knowing the relative dielectric constant of the core $\epsilon_{\text{r,core}} = \epsilon_{\text{eff}}$ in our honeycomb we can first utilize (3.4) to calculate the filling factor δ. Then we can specify the side a of our honeycomb and finally use (3.10) to equate the wall thickness t_{wall} for our honeycomb. In this way we can achieve a honeycomb design with low dielectric core and a high dielectric skin. Since ϵ_{eff} is only dependent on the filling factor, if ϵ_{i} and ϵ_{m} are kept constant, we see that if the honeycomb side a in figure 3.3 increases then ϵ_{eff} is the same but the thickness of the wall is increased.

The design of our honeycomb unit cell should be such that the unit cell is $\lambda/4$ or smaller since we can then assume that the unit cell is effectively a homogeneous structure [39]. It is also preferable that the wall thickness is thin since we then get a low filling factor which reduce the effect on performance.

Chapter 4
Radome Design Method

In order to implement and test the theory to find optimum radome designs previously introduced, we need tools. We believe that radome design is an optimization problem, thus some optimization method is needed. Also, methods to calculate and simulate the radome S-parameters are needed. As mentioned in chapter 1.2 we want to do the calculations in Python and validate the result with finite element method simulation software like HFSS and COMSOL Multiphysics.

4.1 Multilayer Analysis with Transmission Line Theory

Sandwich structures can be analyzed using transmission line theory as suggested in [37]. When using transmission line theory each layer can be seen as a transmission line in cascade with the other layers. Having cascaded transmission lines, it is convenient to use $ABCD$ parameters [24]. If we are able to calculate the $ABCD$ parameters then we can also calculate the reflection S_{11} and the transmission S_{21} from the relations [24].

$$S_{11} = \frac{A + B - C - D}{A + B + C + D} \tag{4.1}$$

$$S_{21} = \frac{2}{A + B + C + D} \tag{4.2}$$

Assuming that all dielectric layers have no magnetic properties, i.e the relative dielectric constant $\mu_{\mathrm{r}} = 1$, then for a m-layer radome, where $i = 0, 1, 2, ..., m-1, m$, with air on either side we can get the $ABCD$ parameters from [37]

$$\begin{aligned}\begin{bmatrix} A & B \\ C & D \end{bmatrix} = &\begin{bmatrix} \cos\xi_1 & \mathrm{j}\bar{Z}_1^{\mathrm{TM,TE}}\sin\xi_1 \\ \mathrm{j}\dfrac{\sin\xi_1}{\bar{Z}_1^{\mathrm{TM,TE}}} & \cos\xi_1 \end{bmatrix}\begin{bmatrix} \cos\xi_2 & \mathrm{j}\bar{Z}_2^{\mathrm{TM,TE}}\sin\xi_2 \\ \mathrm{j}\dfrac{\sin\xi_2}{\bar{Z}_2^{\mathrm{TM,TE}}} & \cos\xi_2 \end{bmatrix}\cdots \\ &\cdots\begin{bmatrix} \cos\xi_{m-1} & \mathrm{j}\bar{Z}_{m-1}^{\mathrm{TM,TE}}\sin\xi_{m-1} \\ \mathrm{j}\dfrac{\sin\xi_{m-1}}{\bar{Z}_{m-1}^{\mathrm{TM,TE}}} & \cos\xi_{m-1} \end{bmatrix}\begin{bmatrix} \cos\xi_m & \mathrm{j}\bar{Z}_m^{\mathrm{TM,TE}}\sin\xi_m \\ \mathrm{j}\dfrac{\sin\xi_m}{\bar{Z}_m^{\mathrm{TM,TE}}} & \cos\xi_m \end{bmatrix}\end{aligned} \tag{4.3}$$

where

$$\bar{Z}_i^{\mathrm{TM}} = \frac{\sqrt{\epsilon_{\mathrm{r},i} - \sin^2\theta}}{\epsilon_{\mathrm{r},i}\cos\theta}$$

is the impedance of the TM polarized wave normalised to the impedance in air,

$$\bar{Z}_i^{\mathrm{TE}} = \frac{\cos\theta}{\sqrt{\epsilon_{\mathrm{r},i} - \sin^2\theta}}$$

is the impedance of the TE polarized wave normalised to the impedance in air, and

$$\xi_i = \frac{2\pi d_i}{\lambda_0}\sqrt{\epsilon_{\mathrm{r},i} - \sin^2\theta}$$

In the special case of an A-Sandwich and a TE wave (4.3) simplifies to

$$\begin{bmatrix} A & B \\ C & D \end{bmatrix} = \begin{bmatrix} \cos\xi_1 & \mathrm{j}\bar{Z}_1^{\mathrm{TE}}\sin\xi_1 \\ \mathrm{j}\dfrac{\sin\xi_1}{\bar{Z}_1^{\mathrm{TE}}} & \cos\xi_1 \end{bmatrix} \begin{bmatrix} \cos\xi_2 & \mathrm{j}\bar{Z}_2^{\mathrm{TE}}\sin\xi_2 \\ \mathrm{j}\dfrac{\sin\xi_2}{\bar{Z}_2^{\mathrm{TE}}} & \cos\xi_2 \end{bmatrix} \times \begin{bmatrix} \cos\xi_1 & \mathrm{j}\bar{Z}_1^{\mathrm{TE}}\sin\xi_1 \\ \mathrm{j}\dfrac{\sin\xi_1}{\bar{Z}_1^{\mathrm{TE}}} & \cos\xi_1 \end{bmatrix} \tag{4.4}$$

and in the special case of the single slab we get

$$\begin{bmatrix} A & B \\ C & D \end{bmatrix} = \begin{bmatrix} \cos\xi_1 & \mathrm{j}\bar{Z}_1^{\mathrm{TE}}\sin\xi_1 \\ \mathrm{j}\dfrac{\sin\xi_1}{\bar{Z}_1^{\mathrm{TE}}} & \cos\xi_1 \end{bmatrix} \tag{4.5}$$

Combining (4.1) and (4.2) with (4.3) we can calculate the reflection and transmission for any arbitrary multilayer dielectric structure versus for example frequency. We can then use an optimization algorithm to minimize (4.1) or maximize (4.2).

4.2 Optimization Algorithms

When optimizing multidimensional problems, like the function (4.3) for multilayer sandwiches, optimization algorithms are of great help. An example of a two-dimensional sandwich radome problem with multiple local minima is shown in figure 4.1 which represents a C-sandwich radome with fixed dielectric constants, where the maximum reflection of the TE or TM (whichever is largest) is calculated as a function of thickness of skin and core.

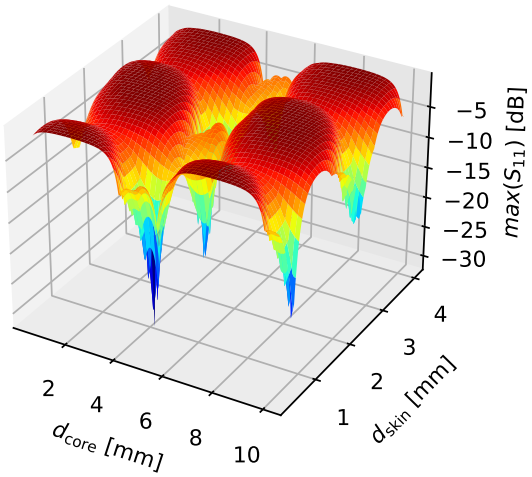

Figure 4.1: Example of a two-dimensional problem with multiple local minima, suitable to be solved with the Differential Evolution algorithm.

In many situations, including radome design, the problem has many more dimensions than the example in figure 4.1. When considering optimization problems with many parameters, other optimization methods than brute force search algorithms are needed. For a brute force search, all possible solutions are iterated through. This means that for a brute force search algorithm with a parameters and n possible steps of each parameter, the time complexity will be $O(n^a)$. The advantage with the brute force search is, however, that we are guaranteed to find the global minimum, which makes it suitable when we are only optimizing for a few parameters or the number of steps are very limited.

The Differential Evolution Algorithm is a metaheuristic nature inspired genetic algorithm, that was invented by Rainer Storn and Kenneth Price in 1997 [40]. Metaheuristic means that, in contrast to the brute force algorithm, it only does a partial search [41], which can decrease the computation time dramatically. It therefore has a very different approach and is much more suitable when optimizing for global multi-dimensional problems. Furthermore, the advantage with the Differential Evolution Algorithm compared to other algorithms for multidimensional problems is that it does not require the problem that should be optimized to be differentiable since it does not use the information of derivatives [42]. Also, the likelihood that the optimization ends up in the global minima has been reported high [40], which makes it a very reliable algorithm as well as higher efficiency than

other evolutionary algorithms has been reported [40]. However, the Differential Evolution Algorithm is stochastic [42] and one is not entirely guaranteed to end up in the absolute global minimum. This means that the optimized result might differ from one time to another.

The basic idea of the Differential Evolution Algorithm is that, given a base population where each individual of the population represents a possible solution to the problem, this population experiences an amount and certain types of mutations. The mutated population then represents the children and the base population represents the parents. Then the parents and their children are compared and in this way the child might replace a parent only if it is "fitter" (more optimized) than the parent [43]. In Python it is possible to use `scipy.optimize.differential_evolution`. In order to increase the probability to end up in a global minimum one can increase the population size, increase the degree of mutation and decrease the amount of recombination [44]. The population size should be directly proportional to the dimension [42]. The recombination value decides the amount of mutated individuals in the population that are allowed to continue to the next generation [44]. Increasing the probability with a solution at the global minimum with this method is of course at the cost of computation time.

A simple high level example of how a Differential Evolution algorithm could be implemented is as follows, which is based on the Differential Evolution Algorithm implemented by [43]: Each individual in the population has initially a random set of parameters that gives a certain solution to the function that we want to optimize. For each candidate j from the population, we can then pick three other randomly chosen individuals (a, b and c) from the population and do a mutation on individual a as a result of the difference between individuals b and c times some mutation constant. The amount of mutation is decided upon the mutation constant which gives a larger or smaller degree of mutation as mentioned earlier. Then a crossover between the mutated individual and candidate j is done. Lastly the crossover result is compared with candidate j. If the crossover result is better than candidate j then candidate j is replaced with the crossover result. A flow chart to illustrate this is shown below.

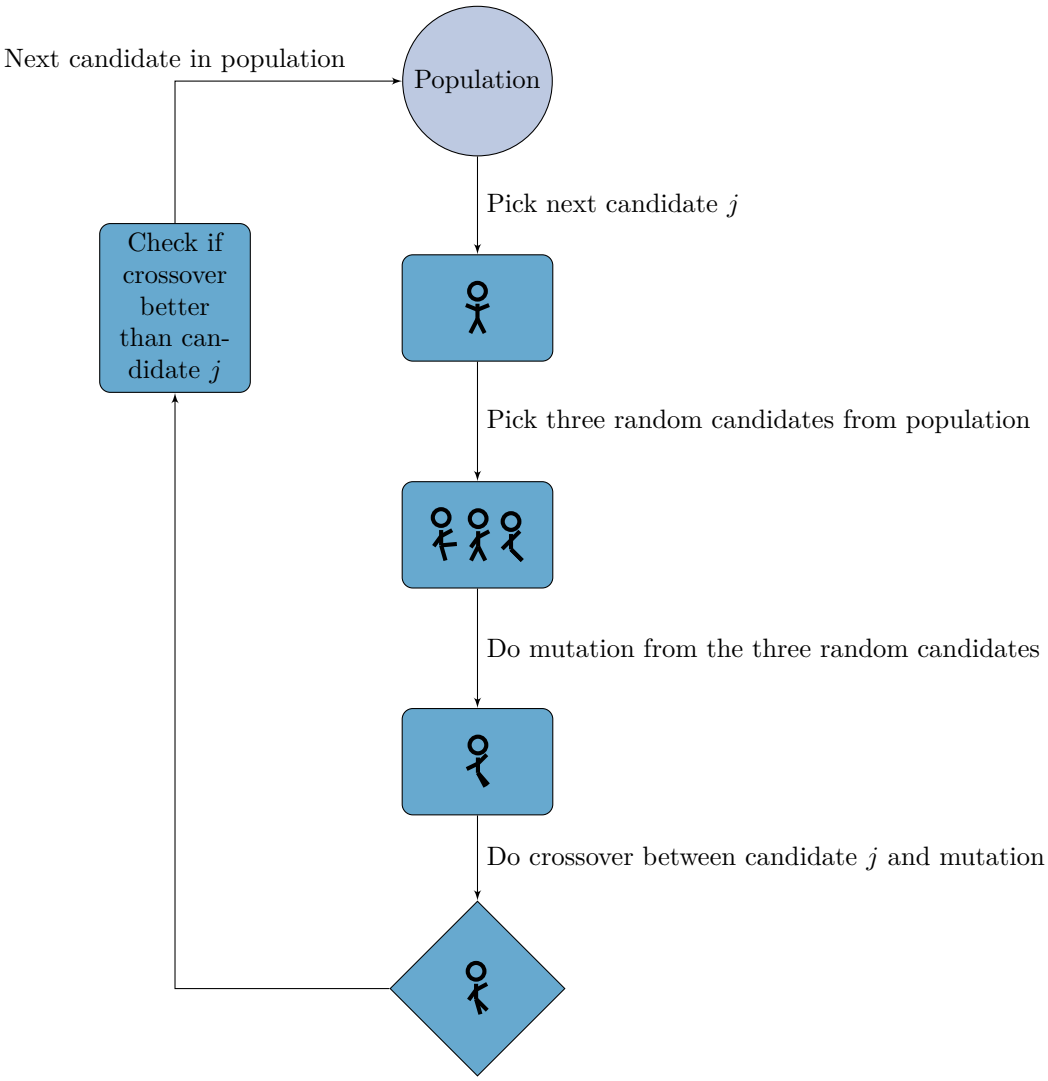

When we have gone through the entire population, where some of the individuals now have mutated towards a better result, then we do the same procedure again on the entire population, and some individuals will then mutate again towards an even better result. This is iterated until the result converges or we have reached a maximum defined number of iterations.

4.2.1 Optimization and Transmission Line Theory

When optimizing the reflection (4.1) through (4.3) of a radome for wide angles, then we need to optimize for all the angles simultaneously, i.e. that we cannot necessarily just focus on one angle of incidence during the optimization and hope that the other angles of interest will fullfill our requirements. Instead, let us say

that we have an m-layer radome with the parameters $\epsilon_{\mathrm{r},0}, \epsilon_{\mathrm{r},1}, ..., \epsilon_{\mathrm{r},m-1}, \epsilon_{\mathrm{r,m}}$ and $d_0, d_2, ..., d_{m-1}, d_m$. Then for each set of parameters, if our radome needs to have low reflection for n angles then our numerical optimization method is to evaluate each angle θ_k, $k = 0, 1, 2, ..., n-1, n$. We can then optimize for the angle θ_k that has the worst power reflection in dB. Let us consider an optimization algorithm with I iterations, where each iteration is $i = 0, 1, 2, ..., I-1, I$. This means that the worst reflection to optimize for at iteration i for TE polarization is

$$W_{\mathrm{TE}}(i) = \max(20 \cdot \log |S_{11}^{\mathrm{TE}}(\theta_k)|), \quad k = 0, 1, 2, ..., n-1, n \tag{4.6}$$

For TM polarization the worst reflection at iteration i becomes

$$W_{\mathrm{TM}}(i) = \max(20 \cdot \log |S_{11}^{\mathrm{TM}}(\theta_k)|), \quad k = 0, 1, 2, ..., n-1, n \tag{4.7}$$

Which gives the optimized result F_{TE}

$$F_{\mathrm{TE}} = \min(W_{\mathrm{TE}}) \tag{4.8}$$

if we want to optimize for TE polarization only. And if we want to optimize for TM polarization only then the optimized result becomes

$$F_{\mathrm{TM}} = \min(W_{\mathrm{TM}}) \tag{4.9}$$

It can be useful to be able to optimize for TE and TM polarization simultaneously. In that case the worst reflection at iteration i is either TE or TM polarized. We can then define the worst reflection at iteration i as

$$W_{\mathrm{TE,TM}}(i) = \max(W_{\mathrm{TE}}(i), W_{\mathrm{TM}}(i)) \tag{4.10}$$

In this case the optimized result $F_{\mathrm{TE,TM}}$ becomes

$$F_{\mathrm{TE,TM}} = \min(W_{\mathrm{TE,TM}}) \tag{4.11}$$

We can see with an m-layer radome in (4.3) that if m is large and each layer has its own unique $\epsilon_{\mathrm{r},i}$ and d_i, then will the space to optimize for be very large, thus the Differential Evolution algorithm is a good choice. However for a very few layers m with for example fixed $\epsilon_{\mathrm{r},i}$ then a brute force search can be a better choice since the compute time will be reasonable and we are guaranteed to find the global minimum.

4.3 Finite Element Method

In order to validate the results from our optimizations done in python we require an electromagnetic simulation software. For this project we have chosen to use Ansys HFSS and COMSOL Multiphysics. HFSS has different solver methods and we have chosen to use the FEM-solver [45] in order to build up our model and simulate the electromagnetic properties. The FEM solver works in such a way that it divides the whole structure, such as the radome, into smaller parts called "finite elements" and reconnects them via nodes. For a 2D system these elements

are often triangular and for a 3D system the shape can vary and be for example tetrahedrons and hexahedrals [46]. The division of these elements is done via what is called a "mesh" [46] which controls how many elements there are and can be adjusted in roughness. A more rough mesh means fewer elements and faster computing time but also a less accurate result.

In order to produce a solution the FEM solver calculates the differential equation for the boundary value [47], in our case for electromagnetism, in each individual element and this is then combined in order to create a solution for the whole system. This method can be applied to a variation of different problems and is not limited to electromagnetism but also for e.g acoustics, fluid dynamics and thermal conduction in order to calculate for example air flow and heat transmission.

4.4 Methodology

We define our radome design methodology for a certain radome type as follows:

- Investigate a type of radome that seems promising for wide-angle use based on previous work in order to develop a design methodology for that type of radome.
- With a certain radome type we can narrow the number of parameters and boundaries for our calculation of the radome performance.
- Measure the relative permittivity for the material used in the additive manufacturing process.
- Calculate in Python with help from chosen theory and do an optimization in order to find the best performance.
- Validate the optimized result in HFSS.
- Full simulation with COMSOL Multiphysics.
- If materials are available do a measurement for final validation.

Often the last step is difficult to implement due to eventually high prototype expenses and/or long production time from the vendors. In order to produce a prototype with the time and resources that are available to us we therefore chose to focus on production via additive manufacturing.

We first simulated and optimized the radome designs with the Python and HFSS simulations in order to find an optimized structure. This was done for the half-wavelength, A-sandwich, honeycomb core radome and the B-sandwich designs. Due to limitations in time and resources we could not produce a B-sandwich prototype, this was then evaluated with a full simulation of the antenna gain in COMSOL Multiphysics. This is investigated in chapter 8.

The prototypes that were produced were done via 3D-printed fused filament fabrication [48] with polylactic acid (PLA) as the material of choice. The prototype

that was produced first is a 24 GHz half-wavelength radome that was used as a benchmark and then a $N = 2$ honeycomb core A-sandwich design was produced. These were used in order to validate the simulated results as compared to the measurement performed where the transmission coefficient S_{21} was compared.

4.4.1 Measurement Setup

In figure 4.2 we have the measurement set-up that was used in order to investigate the performance of our prototype, the results was with an Anritsu Vector Network Analyzer (VNA). A distance of 10 cm between the horn opening and the radome was chosen since this gave the most accurate result when comparing different measurement distances.

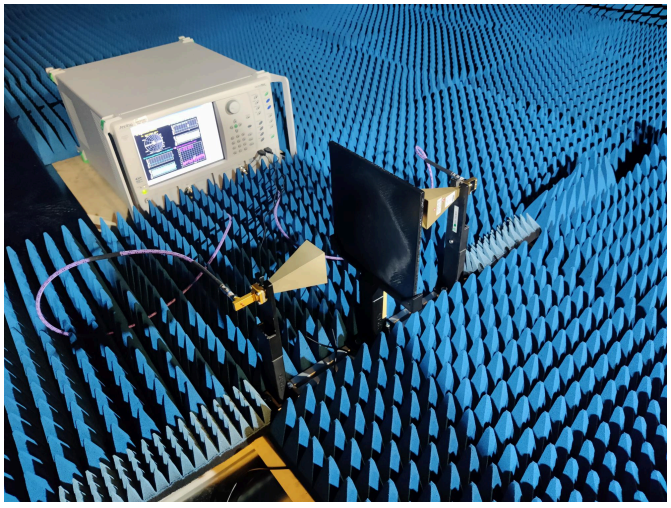

(a)

Figure 4.2: Measurement set-up in an isolated room. The VNA was used in order to measure the S-parameters with horn antennas at 20 dB gain at a distance of 10 cm from the radome.

Chapter 5

Simulations of Half-Wavelength Radomes

In this chapter we present a conventional half-wavelength radome design for 24 GHz and its behaviour at different polarizations and angles of incidence. These simulations are used as a benchmark for the alternative radome designs that are presented in chapter 6.

5.1 Multiples of the Half-Wavelength Slab

As has been shown in (2.25) we have, in theory, zero reflection at normal incidence to the radome if the thickness of the radome d is integer multiples n of half the length of the guided wavelength in the dielectric material. As a first study, a half wavelength slab was simulated in HFSS for a frequency of 24 GHz for a plane wave at normal incidence (i.e. $\theta = 0°$) to the slab. This was done to check if the model that was set up in HFSS was correct. Note that since $\theta = 0°$, TE and TM polarization gives the same result. A slab made of Poly(methyl methacrylate) (PMMA), commonly known as Plexiglas, with a relative permittivity $\epsilon_{\mathrm{r,Plexiglas}} = 3.4$ and a loss tangent $\tan\delta = 0.001$, was chosen. The simulated result for the reflection S_{11} and transmission S_{21} is shown in figure 5.1. Here n is the multiple of the half-wavelength thickness, as previously mentioned in (2.25).

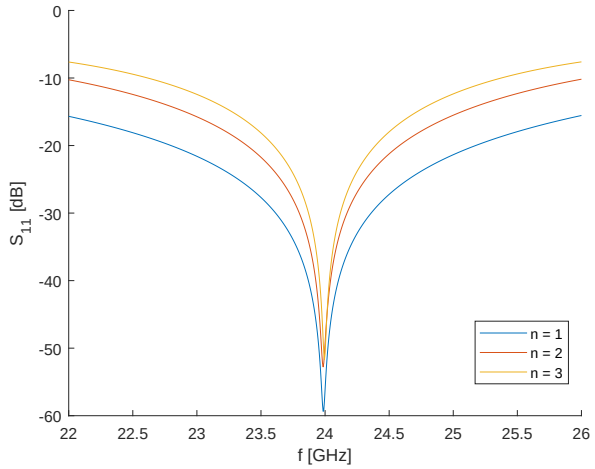

(a)

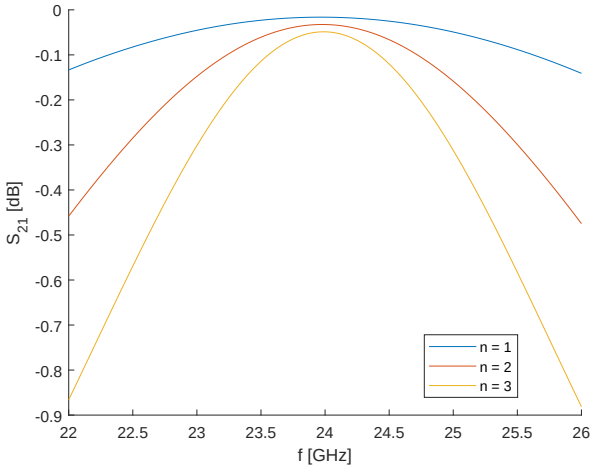

(b)

Figure 5.1: In (a) the reflection S_{11} is plotted at 24 GHz for the half-wavelength slab of Plexiglas with $\epsilon_{\mathrm{r,Plexiglas}} = 3.4$. With an increase in integer n we see a smaller bandwidth and lower gain. In (b) the transmission S_{21} is plotted for the same data and we see the same result that the bandwidth and gain decrease with a higher n.

As expected it is evident that we have highest transmission and lowest reflection at the design frequency of 24 GHz. Also, at closer inspection it is interesting to see that the bandwidth narrows at higher orders n. However, as has been shown in (3.1), the thickness d for which we should have minimum reflection changes with an angle θ of the plane wave. In order to see how the reflection is affected

by the angle of incidence, a simulation for the reflection S_{11} was done in HFSS for a sweep of angles of incidence from 0° to 80°. The reflection versus frequency result for a TE polarized wave is shown in figure 5.2a and the TM polarized case is shown in figure 5.2b. We see for the TE case that the frequency for which we have minimum reflection increases as we increase θ. The reason is that the more the angle of incidence diverge from the normal, the further we stray away from the half-wavelength condition (2.25). However, for the TM case we see a decrease again which is due to the Brewster angle [14, Ch.7]. Also, a plot at the exact frequency of 24 GHz for the angle versus the reflection for both polarization cases is shown in figure 5.2c. We see clearly the Brewster angle for the TM polarized wave at around 60° which is verified using (2.36). From here it is very clear, for the TE case, that already at angles above 20° we have quite high reflections.

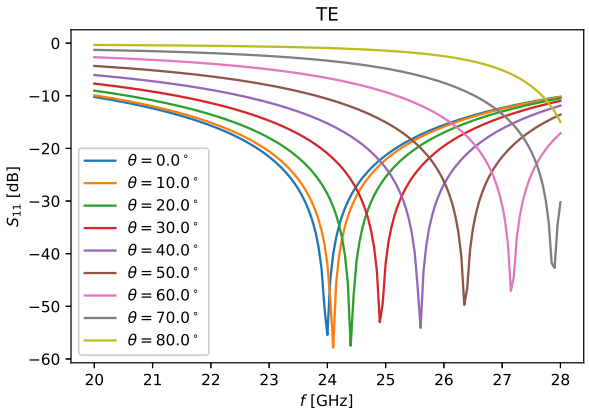

(a)

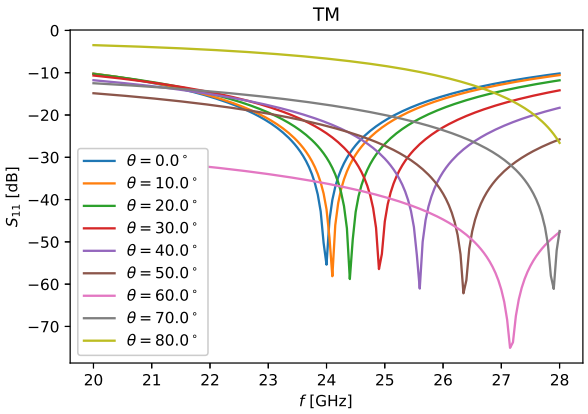

(b)

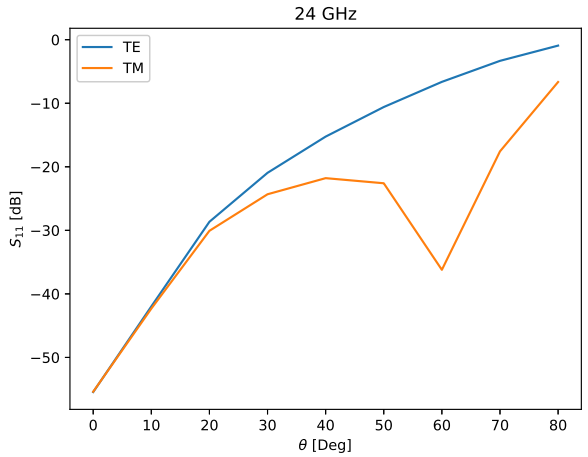

(c)

Figure 5.2: Reflection plots for a 24 GHz single half wave slab. $\epsilon_r = 3.4$, $\tan\delta = 0.001$. (a) shows the TE polarization theta sweep, (b) shows the TM polarization and (c) shows TE and TM at 24GHz over the theta.

Chapter 6
Sandwich Results

In this chapter we investigate the performance of different sandwich structure radomes as shown in figure 3.2. The purpose of this is to compare the performance with different types of sandwich structures to see if we can achieve a wide-angle radome. As mentioned previously our goal for the sandwich design is to keep the reflection below -25 dB for angles of incidence up to 50°, both for the TE and TM polarizations.

For the sandwich designs there are some limitations on the dielectric constant, this since for radome design we use polymers, PCB materials or ceramic materials. These materials range from 2 to 9 in dielectric constant with some exceptions where they go down to 1.05 and up to around 12 [22, 16].

6.1 The A-Sandwich Optimized for Normal Incidence

As a first comparison between the single half-wavelength slab and the A-Sandwich, (3.2) was used to calculate the optimum core thickness of an A-Sandwich for an angle at normal incidence. In order to make a somewhat fair comparison between the half-wavelength slab simulated in figure 5.2 we modelled an A-Sandwich structure with a skin with a relative dielectric constant $\epsilon_{\mathrm{r,skin}} = 3.4$ and a core with a relative dielectric constant $\epsilon_{\mathrm{r,core}} = 1.5$. Choosing a skin thickness $d_{\mathrm{skin}} = 0.5$ mm and utilizing (3.2) and (3.3) we got an optimum core thickness $d_{\mathrm{core}} = 2.3$ mm. The A-Sandwich radome was simulated in HFSS with the result shown in figure 6.1. Figure 6.1a shows the reflection for a TE polarized plane wave versus frequency for angles from 0° to 80°. Figure 6.1b shows the reflection versus angle of incidence at exactly 24 GHz for both the A-Sandwich together with the half-wavelength slab that was plotted earlier in figure 5.2. The angles of incidence were swept at a step size of 10°.

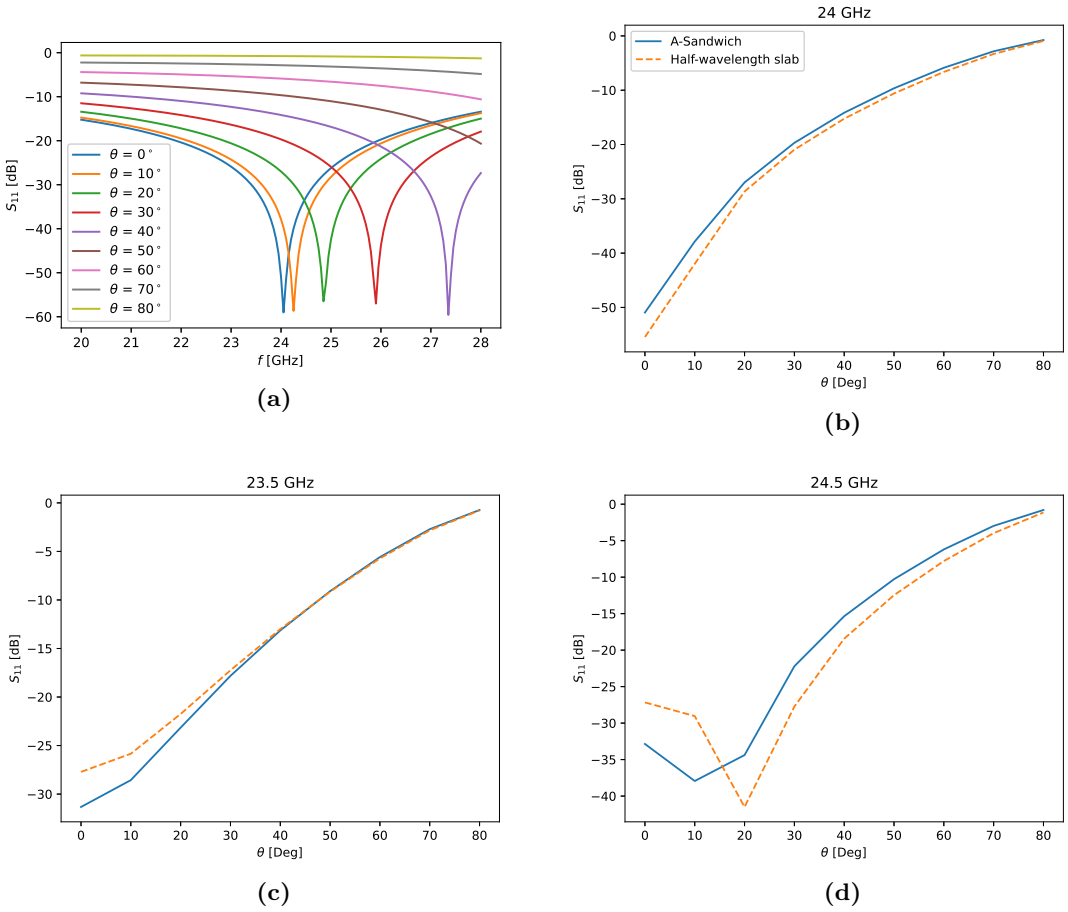

Figure 6.1: Reflection plot of an A-Sandwich 24 GHz simulation in HFSS. It has a skin with $\epsilon_{\mathrm{r,plexiglass}} = 3.4$, $d_{\mathrm{skin}} = 0.5$ mm, and a core with $\epsilon_{\mathrm{r,core}} = 1.5$, $d_{\mathrm{core}} = 2.3$ mm.

It can be seen from figure 6.1b that at exactly 24 GHz it is still better to use a half-wavelength slab. However, comparing figure 6.1a with figure 5.2a we see that the bandwidth is broader for all angles for the A-Sandwich. This means that the A-Sandwich could potentially, at some angles, have better performance than the half-wavelength slab at frequencies diverging by a few hundred MHz from the operating frequency. This can bee seen in figures 6.1c and 6.1d, where the reflection has been plotted at 23.5 GHz and 24.5 GHz respectively. This means that instead of optimizing only for $\theta = 0°$ it can be beneficial to utilize the broader bandwidth of the A-Sandwich.

6.2 Stacks of Multiple A-Sandwiches for Improved Angular Performance

It is clear from the previous section that it is needed to optimize for all angles of incidence of interest in order to achieve a satisfying result with low reflection for a broad range of angles of incidence. Utilizing the broader band of the A-Sandwich compared to that of the half-wavelength slab might be a path to choose for a wide angle design. Further, we now investigate the A-sandwich design optimized for larger angles of incidence.

As has been shown, we can use (4.3) together with (4.1) and (4.2) to calculate reflection and transmission for a flat arbitrary multilayer radome design. In [16] it has been shown that designing a radome by a multiple N of A-Sandwiches stacked upon each other should obtain a very broad frequency band. Our motivation in investigating this method is that a broad frequency band should give low reflections for wide angles as well. An illustration of this design method is shown in figure 6.2. This means that we have three different thicknesses of materials:

- External skin with thickness $d_{\text{skin,ext}}$ and dielectric constant $\epsilon_{\text{r,skin}}$
- Internal skin with thickness $d_{\text{skin,int}} = 2d_{\text{skin,ext}}$ and dielectric constant $\epsilon_{\text{r,skin}}$
- Core with thickness d_{core} and dielectric constant $\epsilon_{\text{r,core}}$

We have chosen to focus on the TE polarization since this is worse for larger angles of incidence than the TM polarization due to the lack of Brewster angle [16]. Each A-Sandwich in the stack has one core and this means that we have N number of cores in a N stack A-Sandwich. Since we consider TE polarization, then we can use (4.4) and define for a $N = 1$ core A-sandwich

$$\begin{aligned}\begin{bmatrix} A & B \\ C & D \end{bmatrix}_1 = \begin{bmatrix} \cos\xi_1 & \mathrm{j}\bar{Z}_1^{\mathrm{TE}}\sin\xi_1 \\ \mathrm{j}\dfrac{\sin\xi_1}{\bar{Z}_1^{\mathrm{TE}}} & \cos\xi_1 \end{bmatrix} \begin{bmatrix} \cos\xi_2 & \mathrm{j}\bar{Z}_2^{\mathrm{TE}}\sin\xi_2 \\ \mathrm{j}\dfrac{\sin\xi_2}{\bar{Z}_2^{\mathrm{TE}}} & \cos\xi_2 \end{bmatrix} \\ \times \begin{bmatrix} \cos\xi_1 & \mathrm{j}\bar{Z}_1^{\mathrm{TE}}\sin\xi_1 \\ \mathrm{j}\dfrac{\sin\xi_1}{\bar{Z}_1^{\mathrm{TE}}} & \cos\xi_1 \end{bmatrix} = M\end{aligned} \tag{6.1}$$

This means that for a N number of cores we get

$$\begin{bmatrix} A & B \\ C & D \end{bmatrix}_N = M^{\mathrm{N}} \tag{6.2}$$

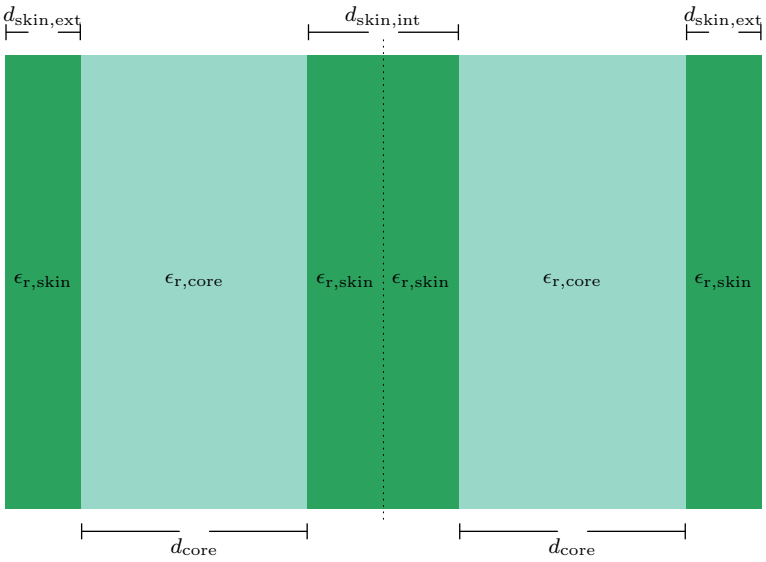

Figure 6.2: Schematic of $N = 2$ A-Sandwich radome.

In order to retrieve the $ABCD$ parameters for any arbitrary N order A-Sandwich (or B-Sandwich) and plot the resulting reflection and transmission, we wrote a Python function. This function utilizes (6.2) to retrieve the magnitude of S_{11} and S_{21} in decibel for any N-order stack of A-Sandwiches over a chosen range of frequencies and range of angles. With help from this function, it is easier to calculate and make quick estimations of the reflections and transmissions for a certain design compared to that of using FEM solvers in HFSS or other simulation software. In order to verify that our Python function and HFSS agree, a 4-stack of the A-Sandwich of the type plotted in figure 6.1 was both calculated in Python using transmission line theory as well as simulated in HFSS. In this design we have a $N = 4$ A-Sandwich with $\epsilon_{\text{r,core}} = 1.5$, $\epsilon_{\text{r,skin}} = 3.4$, $d_{\text{skin,ext}} = 0.5$ mm, $d_{\text{skin,int}} = 1.0$ mm and $d_{\text{core}} = 2.3$ mm. The result of the comparison for the TE polarized plane wave is shown in figure 6.3.

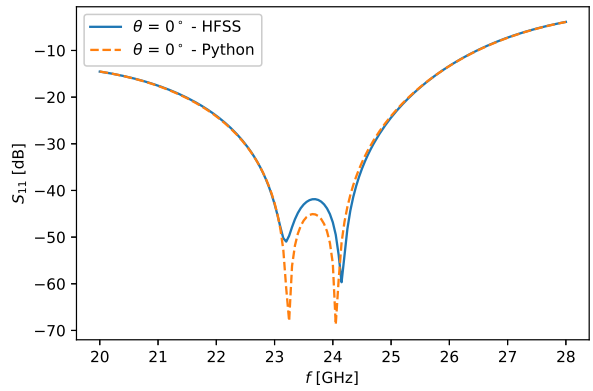

(a)

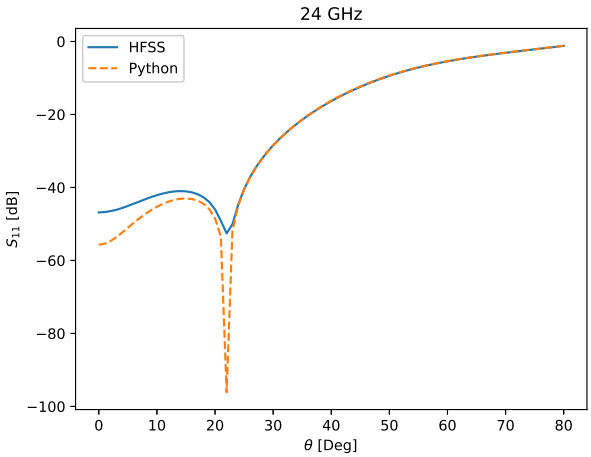

(b)

Figure 6.3: A comparison between Python calculation (dashed line) and HFSS simulation (solid line) for TE polarized plane wave for a $N = 4$ A-Sandwich with $\epsilon_{\mathrm{r,core}} = 1.5$, $\epsilon_{\mathrm{r,skin}} = 3.4$, $d_{\mathrm{skin,ext}} = 0.5$ mm, $d_{\mathrm{skin,int}} = 1.0$ mm and $d_{\mathrm{core}} = 2.3$ mm. (a) The reflection versus frequency for $\theta = 0°$. (b) reflection versus angle of incidence θ.

In figure 6.3a we see the reflection simulated in HFSS and calculated in Python versus frequency for $\theta = 0°$. In figure 6.3b we see the reflection in HFSS and Python versus angle of incidence at 24 GHz. It is clear that the results are very close to each other, but the Python calculation is more optimistic than the HFSS simulation at the extreme values. The reason for the difference in the results is that we have different solver methods, the transmission line theory and the FEM-solver where the transmission line is an exact solution. In both the Python calculation

and the HFSS simulation the step size of the frequency was 0.05 GHz and the step size of the angle of incidence was 1°. In the next section we discuss the qualitative result of this $N = 4$, A-Sandwich using Python. Concluding that the Python function we wrote using transmission line theory agrees well with HFSS, we chose to analyze the wide angle behaviour of the multiple stacks A-Sandiwch using this Python function.

In figure 6.4a, the reflection for TE polarized plane wave versus angle of incidence for different number of N-stacks A-Sandwiches as well as for the half-wavelength slab for comparison is shown. It is clear from this plot that we need a stack of $N = 4$ in order to compete with half-wavelength slab.

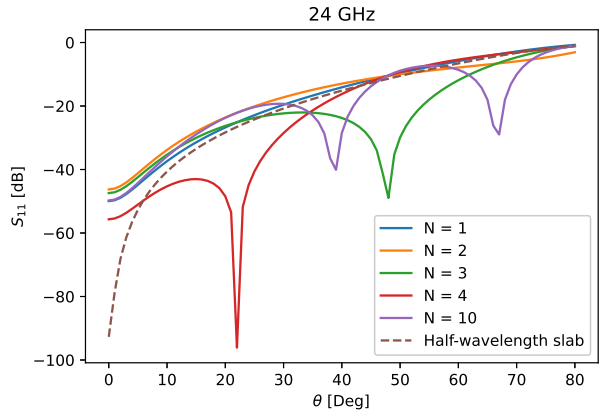

(a)

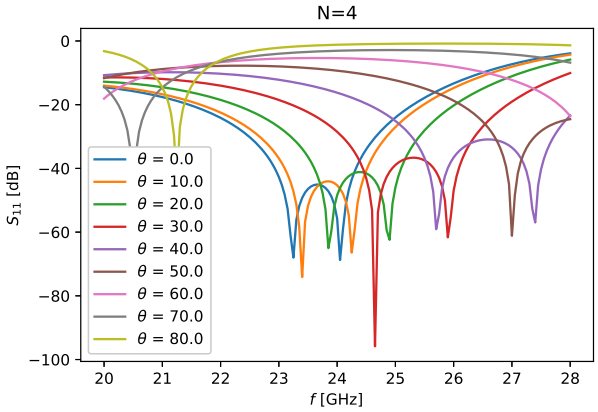

(b)

Figure 6.4: Reflection of an N-stack A-Sandwich radome calculated in Python with $\epsilon_{\mathrm{r,core}} = 1.5$, $\epsilon_{\mathrm{r,skin}} = 3.4$, $d_{\mathrm{skin,ext}} = 0.5$ mm, $d_{\mathrm{skin,int}} = 1.0$ mm and $d_{\mathrm{core}} = 2.3$. (a) The reflection versus frequency for different angles. (b) reflection versus angle of incidence θ for a N =1,2,3,4 and 10 stack A-Sandwich (solid lines) as well as the half-wavelength slab (dashed line) with $\epsilon_{\mathrm{r}} = 3.4$ for comparison.

In figure 6.4b we have plotted the reflection versus frequency for angles between 0° to 80° for the $N = 4$ stack A-Sandwich. Here we clearly see the broad bandwidth for angles of incidence up to 40°, this explains the improved wide angle behaviour compared to that of the half-wavelength slab since the bands of each angle overlaps, to some extend, with each other.

6.2.1 Optimizing the N A-Sandwich

As has been shown previously we can see that by stacking multiple A-Sandwiches, where each of them are designed for minimum reflection at normal incidence angle, we get a broader bandwidth. As a result we also get less reflections for wider angles up to around 40° for a $N = 4$ stack A-Sandwich. However, in order to achieve a better result we chose to see if we could optimize the N-stack A-Sandwich for multiple angles simultaneously.

In many cases we are limited by the choice of dielectric constants for the materials in our radome. From this our approach is that, given some predefined dielectric constants for the two materials, we can calculate the optimal order N of the A-Sandwich stack together with optimal thicknesses of core and skin layers, where $d_{\text{skin,int}} = 2d_{\text{skin,ext}}$ as previously defined. Since only four parameters are considered, namely order N, thickness of the skin $d_{\text{skin,int}} = 2d_{\text{skin,ext}}$, thickness of the core d_{core} and angle of incidence are considered, a simple brute force search algorithm was used in Python. This means that, given some boundaries on the parameters and a certain step size, each possible result is evaluated, which guarantees the best result is found (within the boundaries and limited by the step size of course). Given an array of thicknesses, order N and angles θ, the algorithm finds the lowest maximum reflection for a specified frequency over the range of angles as specified in (4.8), (4.9) and (4.11). The optimization is done on a function utilizing (6.2).

We chose to evaluate N-stack radomes with real materials. First a radome with a core of Rohacell 71HF and a Rogers Duroid 5880 was evaluated. By doing the brute force search over a range of angles from 0° to 60°, N going from 1 to 10 and at a frequency of 24 GHz we found a design optimized for TE polarization, giving $N = 2$, $d_{\text{skin,ext}} = 0.45$ mm ($d_{\text{skin,int}} = 0.9$ mm) and $d_{\text{core}} = 2.9$ mm. In order to verify the correctness of the result the optimized $N = 2$ sandwich was simulated in HFSS as well as plotted using (6.2). The result can be seen in figure 6.5. Even though the sandwich was optimized for TE polarization as defined in (4.8), we chose to plot the reflection of the TM polarized wave as well with both calculation in Python and simulation in HFSS. First of all, it is clear that the transmission line theory used in the Python calculation is still matching well with the HFSS simulation. It is also evident that for the N-stack A-Sandwich it is a good strategy to optimize for TE-polarization since we clearly see that even though we optimized for the TE polarized wave, the TM polarized wave still experience less reflections.

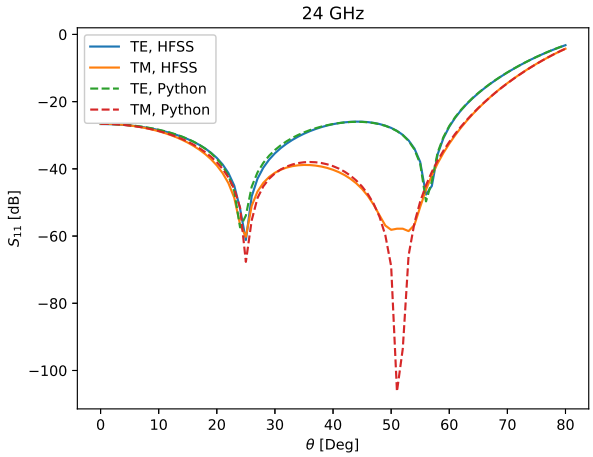

Figure 6.5: Reflection for an $N = 2$ sandwich with a $d_{\text{core}} = 2.9$ mm of Rohacell 71HF $\epsilon_{\text{r}} = 1.09$, loss tangent $\tan\delta_{\text{core}} = 0.0002$, $d_{\text{skin,ext}} = 0.45$ mm of Rogers Duroid 5880 with an $\epsilon_{\text{r}} = 2.2$ and $\tan\delta_{\text{skin}} = 0.0009$ at 24GHz. Both TE and TM polarized wave is plotted from both the result in Python and simulation in HFSS. The sandwich was optimized at 24 GHz for as low reflection as possible for angles going from 0° to 60°.

6.3 B-Sandwich

Another sandwich design that we have chosen to focus on is the B-sandwich design. In figure 6.6 a plot of the reflection at 24 GHz versus angle of incidence calculated with transmission line theory in Python of a B-sandwich with $N = 2$ is shown. The B-sandwich was optimized to minimize the maximum reflection for TE polarization only over the angles of incidence going from 0° to 50° as defined in (4.8). The optimization for the B-Sandwich was done using the Differential Evolution optimizer `scipy.optimize.differential_evolution` as mentioned in section 4.2 with the constraints that $\epsilon_{\text{r,skin}} = \sqrt{\epsilon_{\text{r,core}}}$, $d_{\text{skin,int}} = 2d_{\text{skin,ext}}$ and $\tan\delta = 0.001$. The optimization gave $d_{\text{skin,ext}} = 1.52$ mm, $d_{\text{core}} = 1.45$ mm, $\epsilon_{\text{r,skin}} = 2.6336$ and $\epsilon_{\text{core}} = 6.94$, resulting in a reflection less than -47.7 dB up to a 50° angle of incidence. The boundaries in the optimization for the thicknesses were between 0.3 mm and 10 mm and the boundaries for $\epsilon_{\text{r,skin}}$ was between 2 and 9.

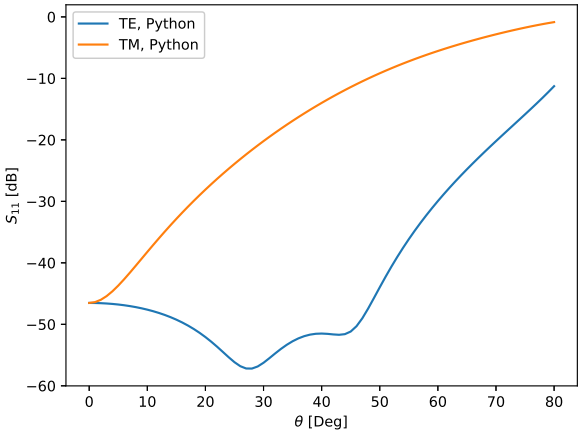

Figure 6.6: Reflection versus angle of incidence of an $N = 2$ B-sandwich optimized for TE polarization with differential evolution algorithm with $\epsilon_{\mathrm{r,skin}} = \sqrt{\epsilon_{\mathrm{r,core}}}$, $d_{\mathrm{skin,int}} = 2d_{\mathrm{skin,ext}}$ and $\tan\delta = 0.001$. Resulting in $d_{\mathrm{skin,ext}} = 1.52$ mm, $d_{\mathrm{core}} = 1.45$ mm, $\epsilon_{\mathrm{r,skin}} = 2.6336$ and $\epsilon_{\mathrm{r,core}} = 6.94$.

The result shown in figure 6.6 shows that for a B-sandwich it is not enough to optimize for TE polarization only since the TM polarization will be worse. For clarity, in order to show that it is enough to optimize for TE polarization for an A-sandwich, we have done a optimization with the differential evolution algorithm for the $N = 2$ A-sandwich as well where again $d_{\mathrm{skin,int}} = 2d_{\mathrm{skin,ext}}$ and $\tan\delta = 0.001$. Obviously for an A-sandwich, the constraint is that $\epsilon_{\mathrm{r,skin}} > \epsilon_{\mathrm{r,core}}$, which was set as a constraint in the optimizer. The boundary for $\epsilon_{\mathrm{r,core}}$ was between 1.09 and 9 and the boundary for $\epsilon_{\mathrm{r,skin}}$ was between 2 and 9. The boundaries for the thicknesses were the same as for the B-sandwich case. This resulted in an A-sandwich with $d_{\mathrm{skin,ext}} = 2.31$ mm, $d_{\mathrm{core}} = 3.76$ mm, $\epsilon_{\mathrm{r,skin}} = 7.51$ and $\epsilon_{\mathrm{r,core}} = 1.09$. The result for the reflection at 24 GHz versus angle for the A-sandwich optimized for TE polarization is shown in figure 6.7. Here we see that even though we optimized for TE polarization, the TM polarization still experience less reflections.

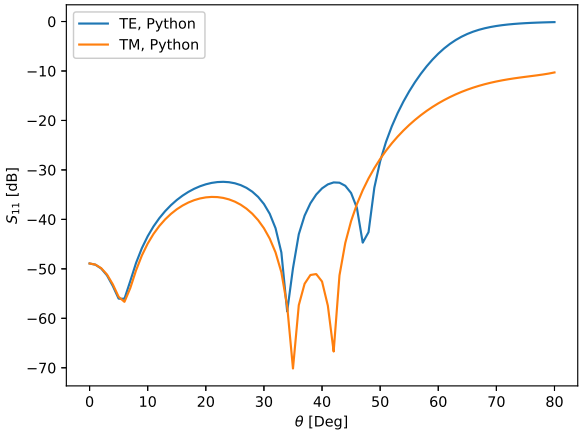

Figure 6.7: Reflection versus angle of incidence of an $N = 2$ A-sandwich optimized for TE polarization with differential evolution algorithm with $\epsilon_{\mathrm{r,skin}} > \epsilon_{\mathrm{r,core}}$, $d_{\mathrm{skin,int}} = 2d_{\mathrm{skin,ext}}$ and $\tan\delta = 0.001$. Resulting in $d_{\mathrm{skin,ext}} = 2.31$ mm, $d_{\mathrm{core}} = 3.76$ mm, $\epsilon_{\mathrm{r,skin}} = 7.51$ and $\epsilon_{\mathrm{r,core}} = 1.09$.

Concluding that an optimization for both TE and TM polarization simultaneously was needed, a differential evolution optimization for a B-sandwich for both polarizations simultaneously was performed as defined in (4.11). Here we use the same set-up, boundaries and constraints as the B-sandwich plotted in figure 6.6 but with the difference that the optimization was done in order to push down the maximum reflection over the angles of incidence $0°$ to $50°$ for both polarizations. This means that the maximum reflection is either TE or TM polarization, whichever has the highest value. The result of the reflection versus angle of incidence at 24 GHz is plotted in figure 6.8.

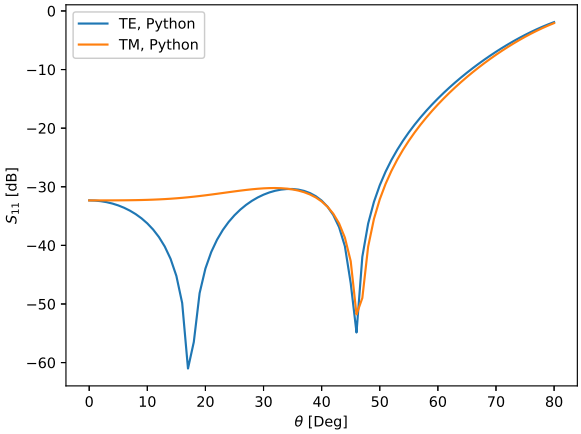

Figure 6.8: Reflection versus angle of incidence of an $N = 2$ B-sandwich optimized for TE and TM polarization simultaneously with the differential evolution algorithm with $\epsilon_{\mathrm{r,skin}} = \sqrt{\epsilon_{\mathrm{r,core}}}$, $d_{\mathrm{skin,int}} = 2d_{\mathrm{skin,ext}}$ and $\tan\delta = 0.001$. Resulting in $d_{\mathrm{skin,ext}} = 1.92$ mm, $d_{\mathrm{core}} = 1.19$ mm, $\epsilon_{\mathrm{r,skin}} = 2.97$ and $\epsilon_{\mathrm{r,core}} = 8.82$.

We see that in this way we are able to keep both the TE and TM polarization reflections low. The cost is that the TE polarization gets worse as compared to the case in 6.6, but the reflection is still under -30 dB for both polarizations. From this we wanted to optimize the B-sandwich further and investigate whether the $N = 2$ sandwich is better as an A- or B-sandwich. In order to find the optimal $N = 2$ sandwich we had to change a few things in the optimization. First, we had to loosen the constraints such that the dielectric constants of the skin and core are not dependent on each other. Secondly, by making the internal skin thickness, $d_{\mathrm{skin,int}}$, independent on the external skin thickness, $d_{\mathrm{skin,ext}}$. The thickness boundaries for $d_{\mathrm{skin,int}}$, $d_{\mathrm{skin,ext}}$ and d_{core} were still between 0.3 mm and 10 mm. The dielectric constant boundaries for $\epsilon_{\mathrm{r,core}}$ between 1.09 and 9 and $\epsilon_{\mathrm{r,skin}}$ were between 2 and 9. The result is shown in figure 6.9.

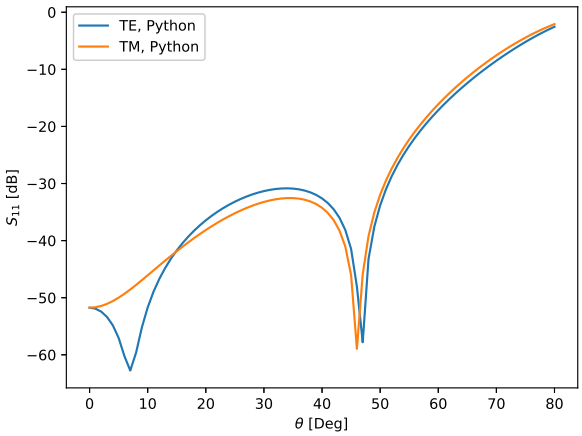

Figure 6.9: Reflection versus angle of incidence of an $N = 2$ sandwich optimized for TE and TM polarization simultaneously with the differential evolution algorithm with $\tan\delta = 0.001$. Resulting in a B-sandwich with $d_{\text{skin,ext}} = 1.80$ mm, $d_{\text{skin,int}} = 3.55$ mm, $d_{\text{core}} = 1.84$ mm, $\epsilon_{\text{r,skin}} = 2$ and $\epsilon_{\text{r,core}} = 8.6$.

We can see, first of all, that the optimization in figure 6.9 results in a B-sandwich, noticing that the B-sandwich outperforms the A-sandwich. We can also see that the result becomes slightly better than the result in figure 6.8 when making $d_{\text{skin,int}}$ and the dielectric constants independent parameters during optimization. However, the difference is small, which indicates that the $\epsilon_{\text{skin}} \approx \sqrt{\epsilon_{\text{core}}}$ rule of thumb and keeping $d_{\text{skin,int}} = 2d_{\text{skin,ext}}$ is a good design method to obtain low reflection for a B-sandwich.

6.3.1 TE & TM Angular Dependence

Another use case that we have not taken into consideration so far is a radome where we optimize for TE and TM differently. This might apply to, for example, a rectangular radome where the elevation is not of the same importance as the azimuth. With this in mind, in figure 6.10 we have plotted two simulations for the $N = 2$ sandwich where TE and TM was optimized for either 50° or 30°. In figure 6.10a the TE mode is optimized for up to 50° and the TM mode for 30°. In figure 6.10b we have the opposite case where TM is optimized up to 50° and TE for 30°.

Figure 6.11 shows the optimization when taking only TE & TM into consideration respectively. Figure 6.11a shows the case for TE up to 50° and figure 6.11b shows the TM mode optimized for up to 50°. From this we can see how the two different optimizations are affected when optimizing over angles of incidence.

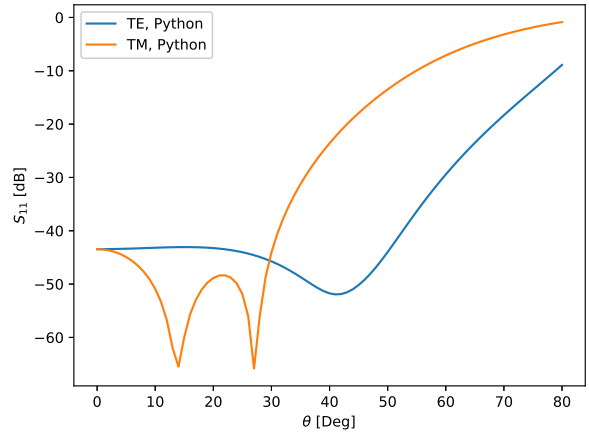

(a)

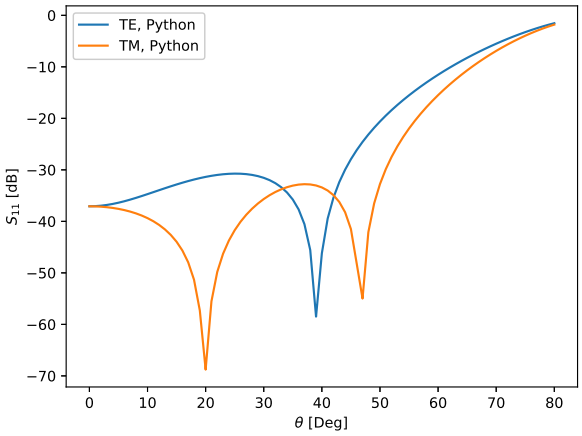

(b)

Figure 6.10: In (a) we have TE optimized for 50° and TM for 30°. Here we get $\epsilon_{\mathrm{r,core}} = 6.92$, $\epsilon_{\mathrm{r,skin}} = 2.03$, $d_{\mathrm{skin,ext}} = 1.72$ mm, $d_{\mathrm{core}} = 4.33$ mm and $d_{\mathrm{skin,int}} = 3.42$ mm. In (b) we have TM optimized for 50° and TM for 30° with: $\epsilon_{\mathrm{r,core}} = 5.59$, $\epsilon_{\mathrm{r,skin}} = 2.40$, $d_{\mathrm{skin,ext}} = 1.93$ mm, $d_{\mathrm{core}} = 1.78$ mm and $d_{\mathrm{skin,int}} = 3.92$ mm. The loss tangent for every material here is $\delta = 0.001$.

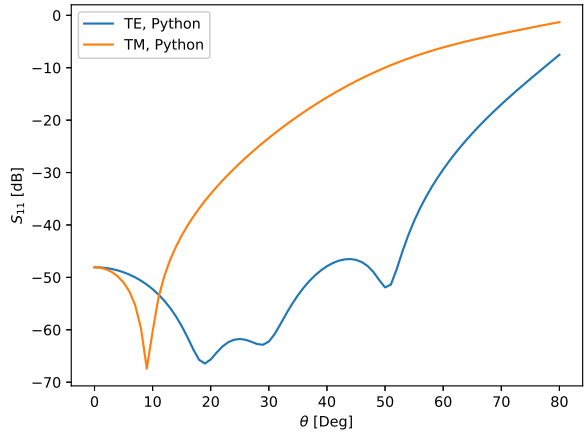

(a)

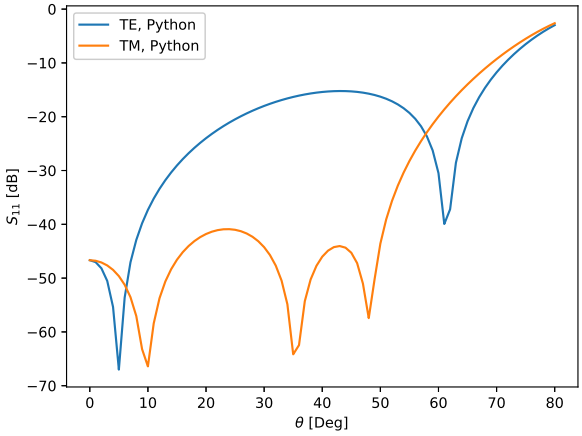

(b)

Figure 6.11: In (a) we have only optimized for TE up to 50°. Here we get $\epsilon_{\mathrm{r,core}} = 5.89$, $\epsilon_{\mathrm{r,skin}} = 2.16$, $d_{\mathrm{skin,ext}} = 2.38$ mm, $d_{\mathrm{core}} = 0.82$ mm and $d_{\mathrm{skin,int}} = 4.81$ mm. In (b) we have only optimized for TM up to 50° with: $\epsilon_{\mathrm{r,core}} = 8.84$, $\epsilon_{\mathrm{r,skin}} = 2.95$, $d_{\mathrm{skin,ext}} = 1.69$ mm, $d_{\mathrm{core}} = 1.63$ mm and $d_{\mathrm{skin,int}} = 7.28$ mm. The loss tangent for every material here is $\delta = 0.001$.

6.4 The Optimized Multilayer Radome

So far we had restrictions on only having two different and alternating materials in our sandwich radome. Since we want to have a symmetric radome then an m-layer radome can have a maximum of $(m+1)/2$ different materials and thicknesses. The

$N = 2$ B-sandwich in figure 6.9 have $m = 5$ layers but only two different materials, even though there is a possibility to have three different materials. Utilizing the Differential Evolution optimization algorithm `scipy.optimize.differential_evolution` in Python, we wanted to investigate an optimum radome with $m = 7$ layers with the possibility of four different materials and four different thicknesses. This radome is neither defined as a B-sandwich nor A-sandwich. Instead it is a multilayer radome as defined earlier. A schematic of a 7-layer sandwich radome is shown in figure 6.12. Here we see that we have four different thicknesses and four different dielectric constants.

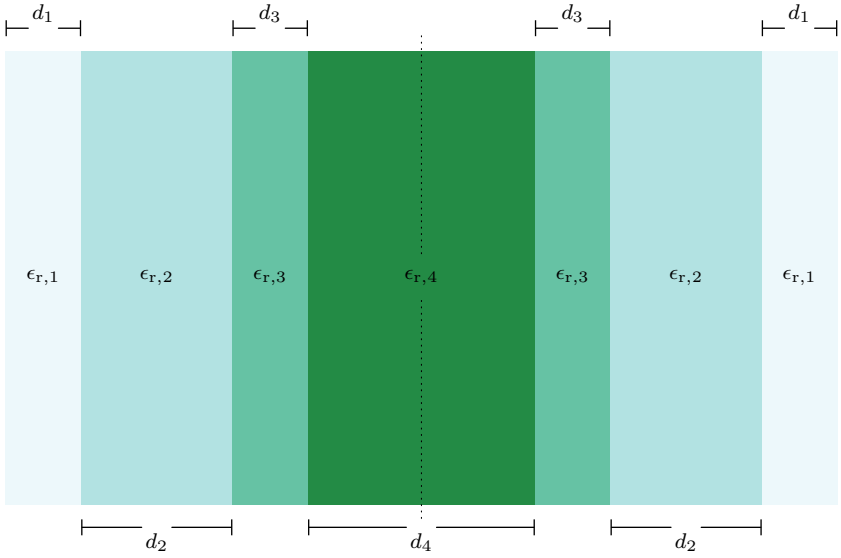

Figure 6.12: Schematic of an example of a 7-layer symmetric radome with a maximum of four different dielectric constants and four different thicknesses. The thicknesses are arbitrary and not to scale.

The result of the reflection versus angle of incidence calculated with transmission line theory in Python for a multilayer sandwich radome with 7 layers optimized with the Differential Evolution algorithm for both TE and TM polarization up to 50° is shown in figure 6.13. With this method we were able to achieve a radome with a reflection under -41.6 dB up to 50° angle of incidence. The obtained values from the optimization for each layer is shown in table 6.1. Each layer had a loss tangent of $\tan\delta = 0.001$. The boundary for each thickness was between 1 mm and 12 mm and the boundary for each relative dielectric constant was between 1.5 and 9.

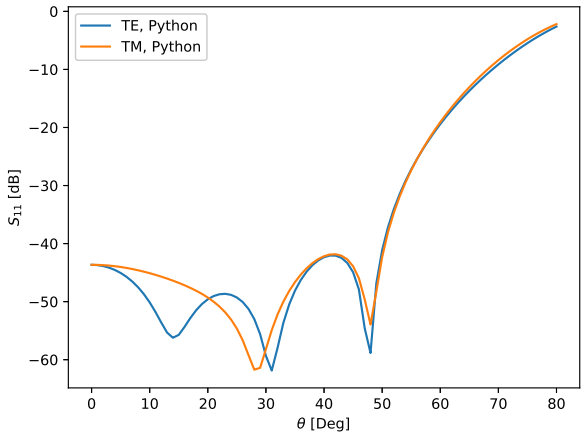

Figure 6.13: Reflection versus angle of incidence for TE and TM polarized waves calculated with transmission line theory for a 7-layer radome optimized with the Differential Evolution algorithm.

Material	**Rel. Dielectric Constant**	**Thickness**
1	$\epsilon_{r,1} = 1.50$	$d_1 = 2.87$ mm
2	$\epsilon_{r,2} = 5.63$	$d_2 = 4.04$ mm
3	$\epsilon_{r,3} = 8.99$	$d_3 = 3.20$ mm
4	$\epsilon_{r,4} = 5.73$	$d_4 = 4.07$ mm

Table 6.1: The obtained values for each of the four materials for a 7-layer radome from an optimization with the Differential Evolution algorithm.

6.5 Tolerances

When optimizing a sandwich structure, an issue might be to which extent it is allowed for the thicknesses of each slab in the sandwich and the dielectric constants of each material to vary. In for example figure 6.9 we might have found the optimized sandwich, but if the thicknesses and the dielectric constants are not allowed to vary too much without degrading the performance, then it might be difficult to fabricate such a radome. In order to give an indication of the limitations for the optimized B-sandwich in figure 6.9, we have plotted in figure 6.14 how the maximum reflection varies with external skin $d_{\text{skin,ext}}$ and core thickness d_{core} in proximity to the global minima that was obtained. And in figure 6.15 we have plotted how the maximum reflection varies with relative dielectric constants ϵ_{skin} and ϵ_{core}. We see from figure 6.14 that the minimum is when $d_{\text{skin,ext}} = 1.80$ mm and $d_{\text{core}} = 1.84$ mm as shown earlier in figure 6.9. $d_{\text{skin,int}}$ is kept constant

at 3.55 mm. However, we see that the maximum reflection quickly increases as the thicknesses diverge from their optimized values. A variation in thickness above approximately 0.05 mm will degrade the maximum reflection to values higher than -25 dB.

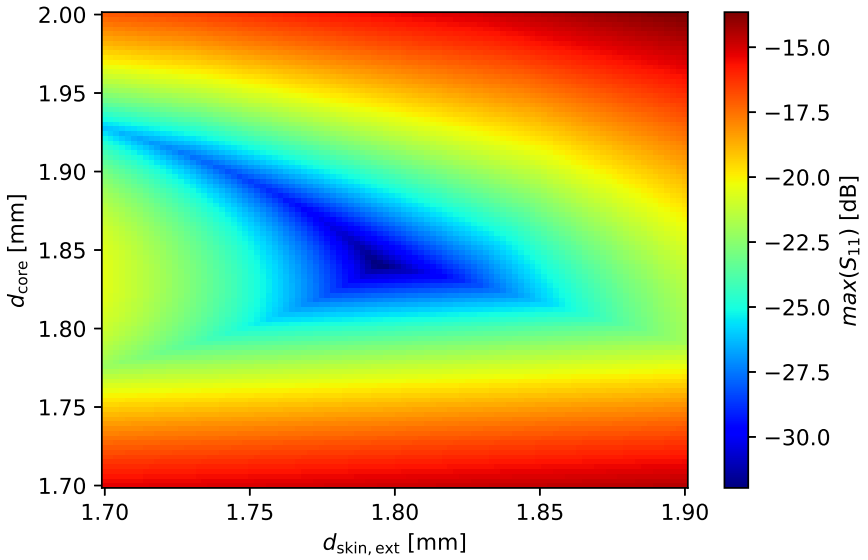

Figure 6.14: 2D plot of the maximum reflection of TE and TM polarized wave as function of d_{core} and $d_{\text{skin,ext}}$.

In figure 6.15 we see that the relative dielectric constant of the external skin ϵ_{core} can vary quite a lot and still keep a maximum reflection below -25 dB while diverging approximately 0.3 from 8.6. However, the relative dielectric constant of the skin ϵ_{skin} is much more sensitive to variations and can not diverge more than 0.1 from 2.0.

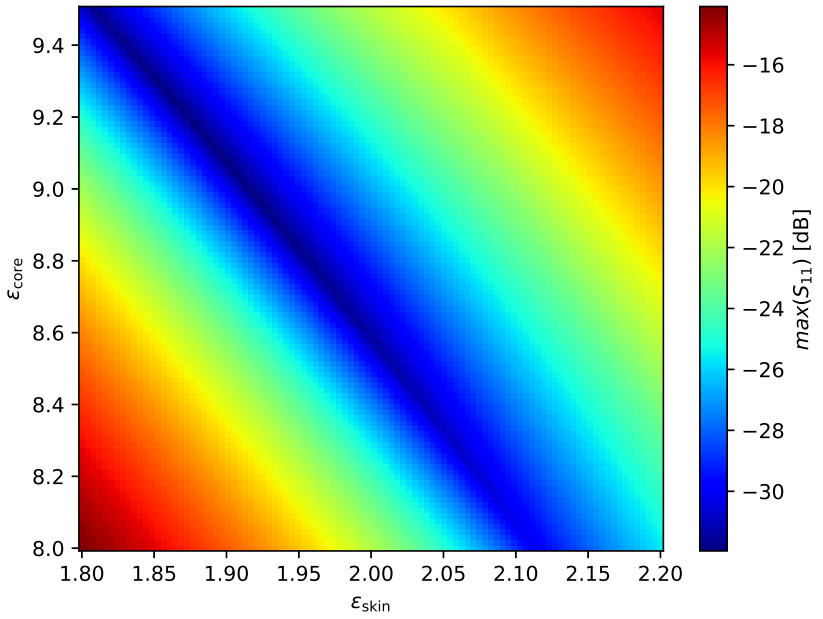

Figure 6.15: 2D plot of the maximum reflection of TE and TM polarized wave as function of ϵ_{core} and ϵ_{skin}.

More interestingly, however, is that we see that in order to obtain minimum reflection, then, for this specific design, ϵ_{core} is a linear function of ϵ_{skin} such that

$$\epsilon_{\text{core}} = k\epsilon_{\text{skin}} + m \tag{6.3}$$

where k and m are constants. This means that keeping the thicknesses constant we can still vary the dielectric constants if we follow (6.3) where k and m easily can be obtained from the plot in figure 6.15. In this particular case $\epsilon_{\text{core}} = -4.91\epsilon_{\text{skin}} + 18.39$. This is a great advantage since we can, after an optimization, utilize (6.3) to find relative dielectric constants that are more close to available materials.

6.6 Summarized results

Within this chapter we have done optimizations on a few radomes designs which have increased performance over angles of incidence up to 50° as compared to the conventional half-wave radome. In figure 6.9 we have shown the optimal $N = 2$ B-sandwich design, in figure 6.7 the optimal $N = 2$ A-sandwich is shown, in figure 6.13 is the 7 layered multi-layer design and lastly in figure 6.10a we can see one of the $N = 2$ B-sandwich design where the two polarizations were optimized differently for a maximum angle of incidence. For convenience and comparison we have summarized these four plots (figures 6.9, 6.7, 6.13 and 6.10a) in figure 6.16.

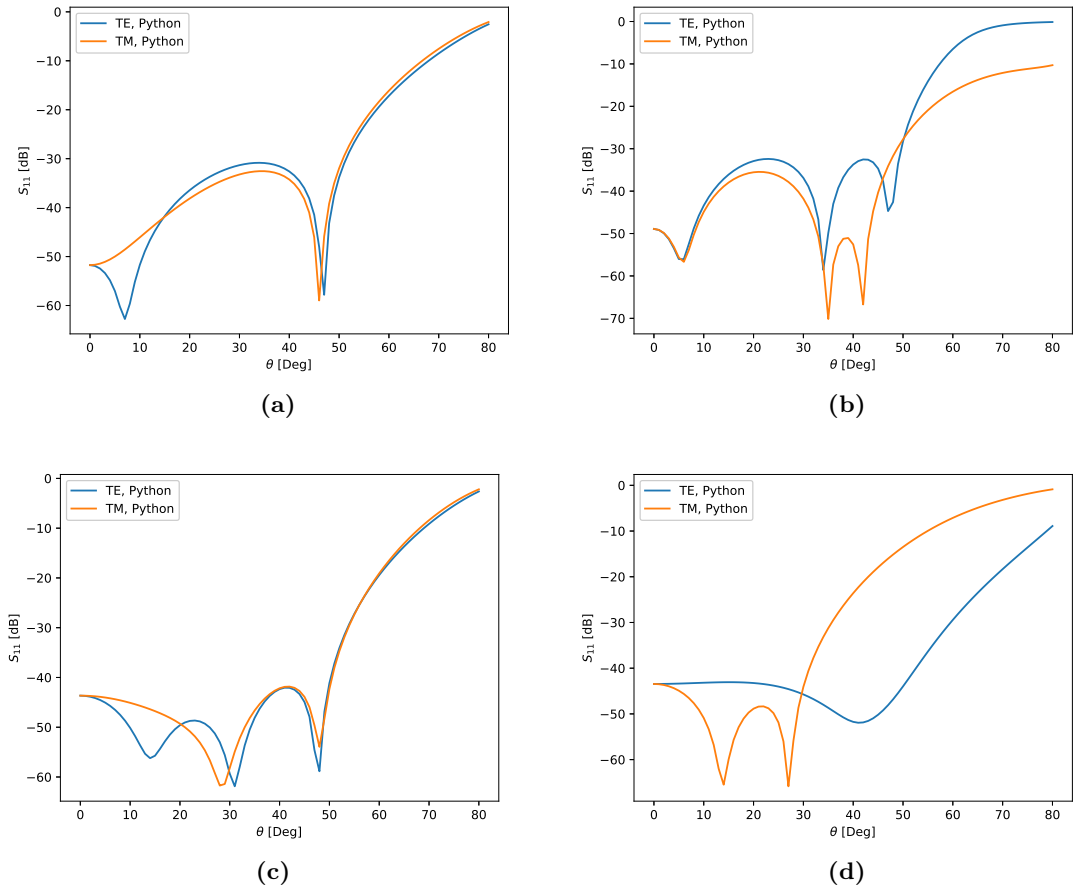

Figure 6.16: (a) $N = 2$ B-sandwich optimal design as in figure 6.9. (b) $N = 2$ optimized A-sandwich as in figure 6.7. (c) 7-Layered multi-layer radome as in figure 6.13. (d) $N = 2$ B-sandwich optimized for 50° TE and 30° TM as in figure 6.10a.

Chapter 7

3D-Prototyping & Measurements

In this chapter we present the process used in order to produce the prototypes as well as the measurement results.

7.1 Honeycomb Prototype

In this project we are investigating a honeycomb design which consists of a single material, in our case 3D printed PLA, where the solid parts and the honeycomb are printed and then assembled. The PLA used is the material measured in table 7.1. Unfortunately, we performed this investigation before the measurement of the dielectric constant as tabulated in table 7.1 and assumed a relative dielectric constant of $\epsilon_r = 2.7$ and loss tangent $\tan\delta = 0.001$, which showed not to be entirely exact.

Nevertheless, with the 3D-print honeycomb method we do not need a separate honeycomb material for our prototype and with this reduce the amount of adhesive layers in the sandwich structure.

We simulated the results of our $N = 2$ A-sandwich honeycomb design in HFSS and compared this to that of the conventional radome with the same measurements and dielectric constants. In figure 7.1 we have used HFSS to simulate two designs of the honeycomb. One with a 2 mm side wall and one with a 3 mm side as well as the conventional A-sandwich radome, which consists of a solid core with the same effective dielectric constant. The effective dielectric constant was calculated via the Maxwell-Garnett equation (3.4). We simulated two different side lengths of the honeycomb unit cell for the 3D-printed model since we had a preferable design at a wall length of 2 mm, however due to limitations in the printing process we had to use a wall length of 3 mm when producing the prototype.

In the results from figure 7.1 we see that the honeycombs perform slightly worse than the conventional radome but we still have good performance over the angle of incidence θ for both honeycomb designs. The advantage of using the honeycomb radome instead of a conventional design is that we can control our own effective dielectric constant of the core and we are then not dependent on finding a specific material with low dielectric constant.

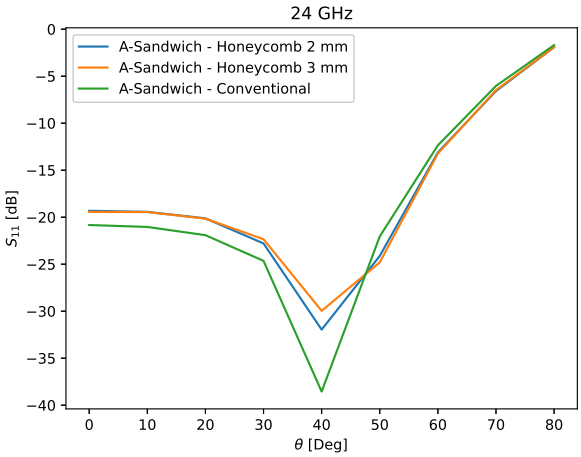

Figure 7.1: Honeycomb $N = 2$ A-sandwich compared to the conventional design. $d_{\text{skin,ext}} = 0.3$ mm, $d_{\text{core}} = 2.6$ mm, $d_{\text{skin,int}} = 0.6$ mm and we have $\epsilon_{\text{r,skin}} = 2.7$ and $\epsilon_{\text{r,core}} = 1.345$.

In figure 7.2 below we can see the printed honeycomb prototype which consists of the three pieces mentioned above and in this model we have a skin of 0.3 mm, a core of 2.6 mm, a filling factor of 28.5%, wall size of 3 mm and according to equation (3.10) this then gives the unit cell $t_{\text{wall}} = 0.4$ mm. The parts consists of two plates with the skin and honeycomb structure and one plate which is the middle section that has a thickness of 2 times that of the skin.

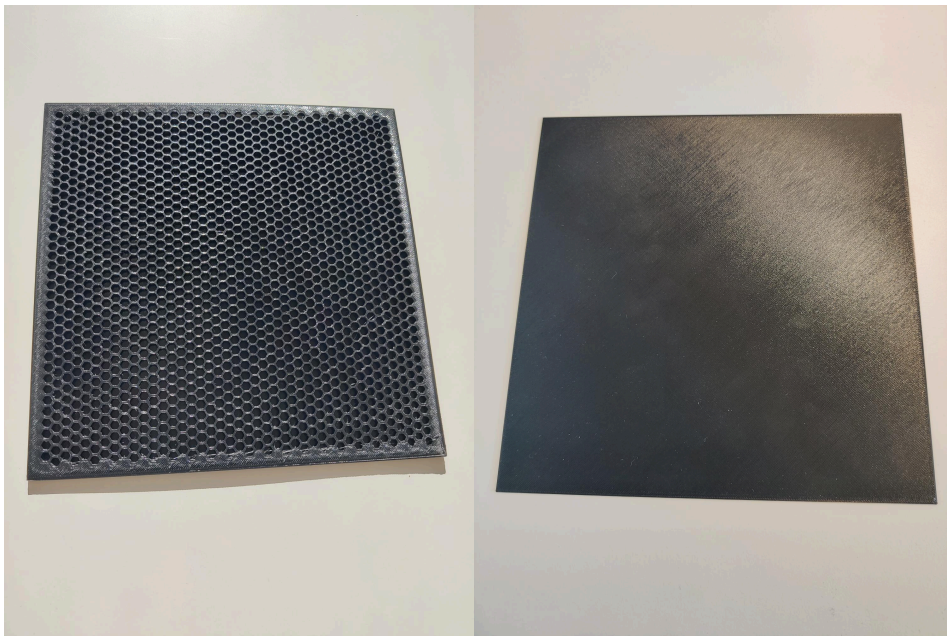

(a) (b)

Figure 7.2: 3D-printed honeycomb A-sandwich radome.(a) Shows the skin and honeycomb core component and. (b) shows the middle skin part which is 0.6 mm thick.

In order to produce the finished radome prototype we need to use an adhesive to combine our pieces and for this we use 3M scotch-weld 76 which has a dielectric constant of 2.32 [49] and an assumed thickness of around 0.05 mm. The reason why we did not print the whole radome in one piece was due to that, with this unit cell size, the threads from the middle layer would bend down into the honeycomb cavities.

Before we used the adhesive on our radome we first tested it out on other 3D-printed PLA pieces shown in figure 7.3a and figure 7.3b so that we could assess the functionality of the adhesive. This test showed that the adhesive gave a fairly thin layer that held together well, even though it could be torn apart but this is outside of the use case for our prototype. When a honeycomb layer was applied onto a surface that had been sprayed with the adhesive and pressed against it we saw that the adhesive forms a thin layer over the cavities of the honeycomb and does not enter. The adhesive was not evenly spread over the whole surface of the PLA samples which might be due to the adhesive being distributed on each of the samples when we tore them apart.

With the radome pieces we sprayed the adhesive onto the middle section and attached the outer honeycomb section, gave it time to dry and then repeated for the other piece. We chose to apply the spray adhesive to the middle section since

it would most likely affect the performance negatively if the adhesive was used on the honeycomb structure since it would enter the honeycomb cavities.

In figure 7.3 below we see the results from the adhesive test as well as the final result of the radome. In figure 7.3b it can be seen that as we mentioned earlier the adhesive does not enter the cavities on the test plate and we assume that the same will apply for the final radome. In figure 7.3c and figure 7.3d the final radome is shown. Here it can be seen that the radome is solid and holds together well. However, it can be seen that one side of the radome is slightly bent; this is due to the bending that occurred in the 3D-printing process. Overall the adhesive worked well for the radome and we take the bend into consideration when performing measurements.

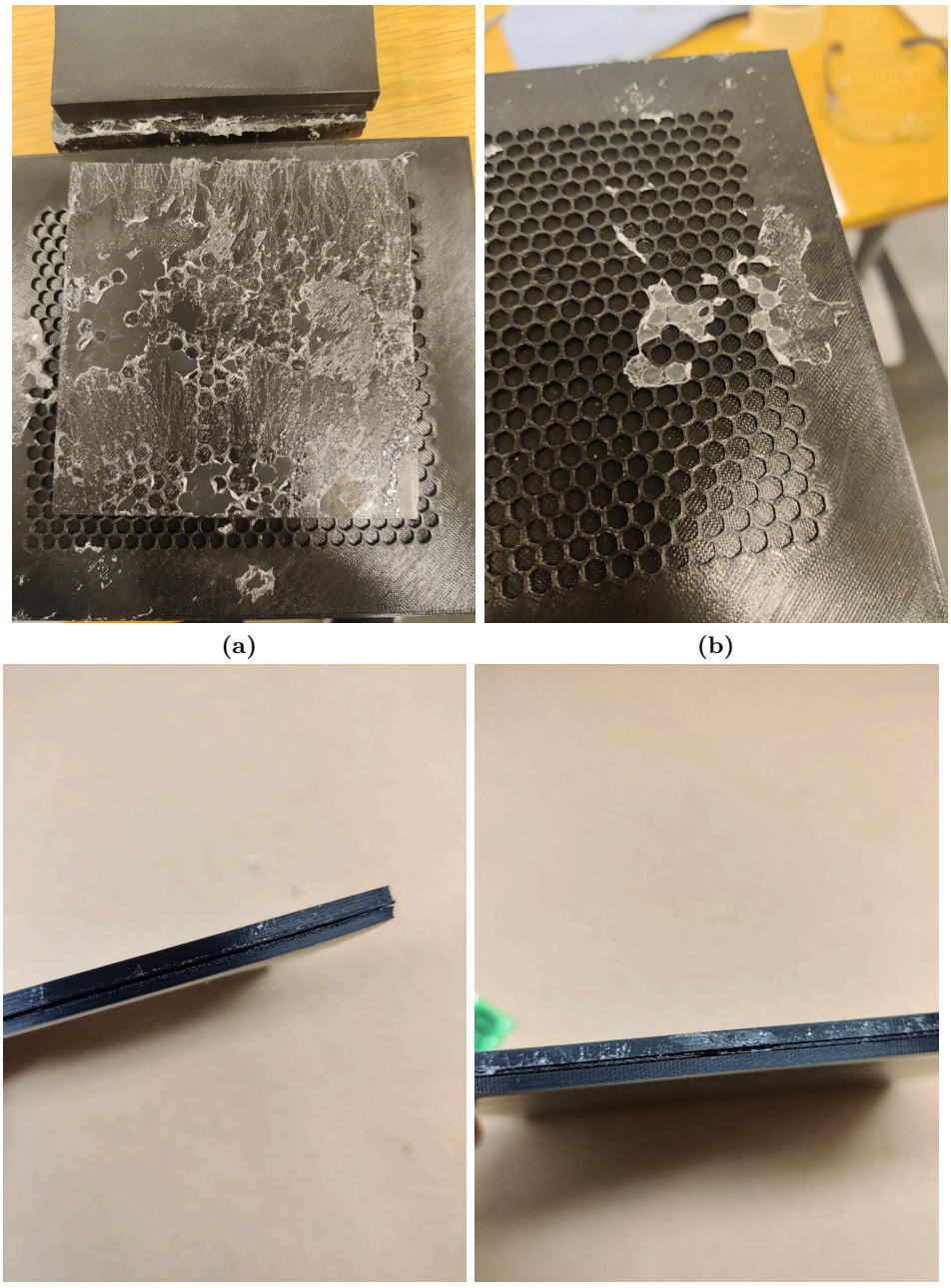

Figure 7.3: Results from the adhesive test as well as the final radome results. Figure (a) shows the flat side which was glued together with (b), we see a mostly uniform layer of the adhesive. In (b) we see the honeycomb test part, here we see that the adhesive does not enter the cavities. Figure (c) and (d) shows the final radome from figure (7.2) glued together.

7.2 Measurement Results

In this section we present the results from the performed measurements of the 3D-printed 24GHz half-wave and honeycomb radome. The measured results are presented with the transmission S_{21} as compared to the previously simulated results which are presented in power reflection S_{11}. This since, due to our measurement method, the reference value is that of full transmission and thus to normalize with a reference we need to use the transmission. In the data for the measurements we first used a reference measurement without the radome. A measurement was then performed with the radome. In the end the measured $S_{21,\mathrm{dut}}$ parameters with the radome was normalized to the measured $S_{21,\mathrm{ref}}$ parameters without the radome as $S_{21} = S_{21,\mathrm{dut}}/S_{21,\mathrm{ref}}$. We also performed a fast Fourier transform on the data to change it from frequency domain to time domain from where we could do time-gating analysis [50].

7.2.1 Half-Wavelength Prototype

The setup described in section 4.4.1 was used in order to measure both the printed honeycomb as well as a half-wave radome. We also used these measurements in order to calculate the real dielectric constant and loss tangent of our PLA. These values are shown in table 7.1.

Rel. Dielectric Constant	**loss tangent**
$\epsilon_{\mathrm{r}} = 2.62$	$\tan\delta = 0.007$

Table 7.1: The measured relative dielectric constant ϵ_{r} and loss tangent $\tan\delta$ of the PLA material.

7.2.2 Half-Wavelength Measurement

A 3D-printed PLA half-wavelength radome was also made, as seen in figure 7.4, which we used in order to further validate the measurement results with a simple structure; the half-wave prototype was used to measure the dielectric constant of PLA in 7.1. In figure 7.5 we see the measured transmission for the 3D-printed half-wave radome compared with the HFSS simulation.

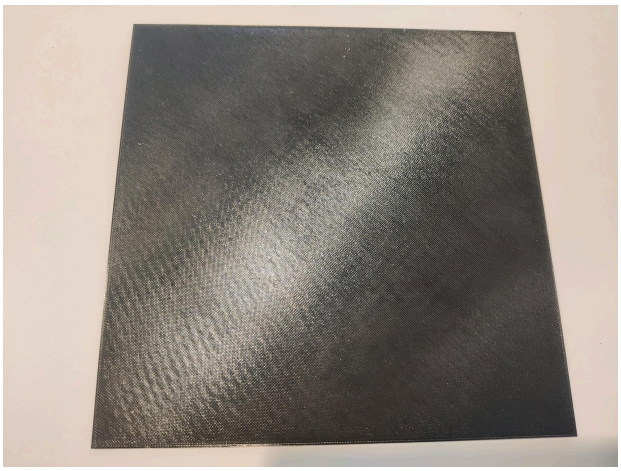

Figure 7.4: Half-wavelength radome prototype, thickness of 3.8mm, 3D printed with PLA.

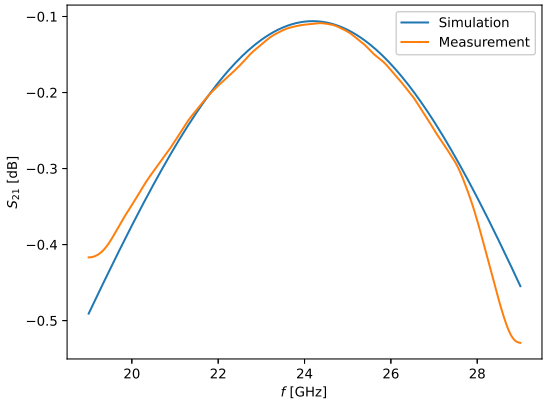

Figure 7.5: Transmission of the measured half-wavelength slab compared to transmission of the same slab in a HFSS simulation. The thickness of the slab is 3.8 mm. $\epsilon_{\mathrm{r,skin}} = 2.62$ and $\tan\delta = 0.007$.

7.2.3 Honeycomb Radome

The honeycomb radome transmission measurement was measured with the setup shown in figure 4.2. As mentioned earlier the measured relative dielectric constant of the PLA material turned out to be 2.62 with a losstangent of 0.007. However, the relative dielectric constant was previously assumed to be 2.7. In figure 7.6 we have plotted the transmission of the measured honeycomb that we designed as well

as the comparison with the transmission of the honeycomb in a HFSS simulation with the dielectric constant and losstangent that we measured from the single slab.

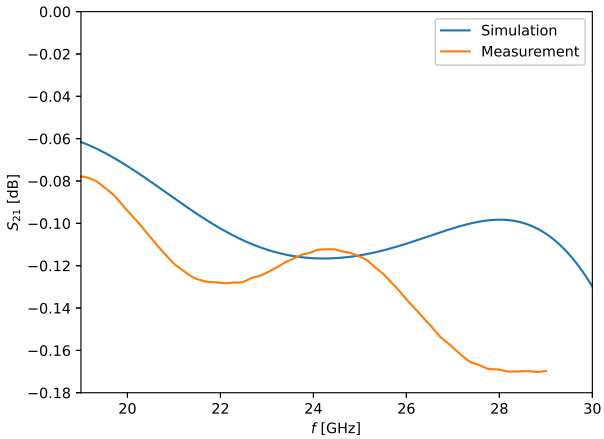

Figure 7.6: The transmission of the measured glued N = 2 Honeycomb A-sandwich compared to HFSS simulation. $d_{\mathrm{skin,ext}} =$ 0.3 mm, $d_{\mathrm{core}} = 2.6$ mm, $d_{\mathrm{skin,int}} = 0.6$ mm. For the measured sample we have $\epsilon_{\mathrm{r,skin}} = 2.62$ and $\tan\delta = 0.007$.

Chapter 8
Finite Radome Simulations

In order to further validate our design method and simulations full wave antenna simulations are needed since here we can investigate, for example, reflections from the substrate, corner effects from the radome as well as the impact from our antenna device.

8.1 Models

The simulations were performed with a 2-dimensional model in COMSOL Multiphysics where lumped ports were used as a source and the radome was build over this and then swept for several angles. The models can be seen in figure 8.1. In figure 8.1a the half-wavelength radome is simulated in COMSOL Multiphysics, this with a dielectric constant of 3.4 and a thickness of 3.39 mm. In figure 8.1b the B-sandwich is modelled, this corresponds to the simulated B-sandwich in figure 6.9. The simulation is performed over angles of incidence from 0° to 50° degrees at 24 GHz. The height of the radome is 12.5 mm over the port, which corresponds to one free space wavelength. The width of the radome is such that there is a gap of 6.25 mm between the ports and the radome, this corresponds to half a free space wavelength. The COMSOL Multiphysics model as well as the dimensions were based on the previous master's thesis by Atefeh Mousavi [28]. Worth to mention is that the first half-circle in figure 8.1 shows the far-field domain border.

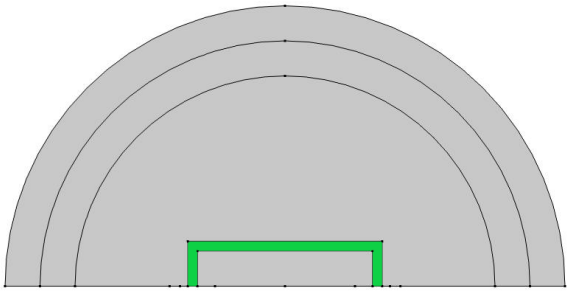

(a)

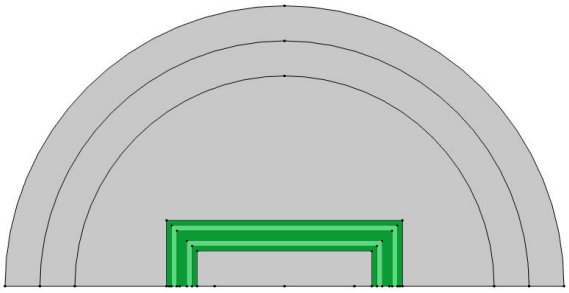

(b)

Figure 8.1: COMSOL Multiphysics models used for antenna simulatons. (a) shows the half-wavelength radome model and (b) illustrates the B-sandwich COMSOL Multiphysics model. The half-wavelength radome is that of the plexiglass halfwave in chapter 5 and the B-sandwich model corresponds to figure 6.9. Here the radomes are the green colored sections, in (b) different colors are used for the different dielectric materials.

8.2 Simulation Results

In order to analyse the designed radomes' performance the maximum gain for each angle of incidence is compared in the case of no radome and in the case with the radome present. In figure 8.2 below we have the maximum gain plotted for each angle θ for the cases of no radome, the half-wavelength radome and the B-sandwich. The half-wavelength radome in this case is the plexiglass radome shown in figure 5.1 and the B-sandwich is shown in figure 6.9.

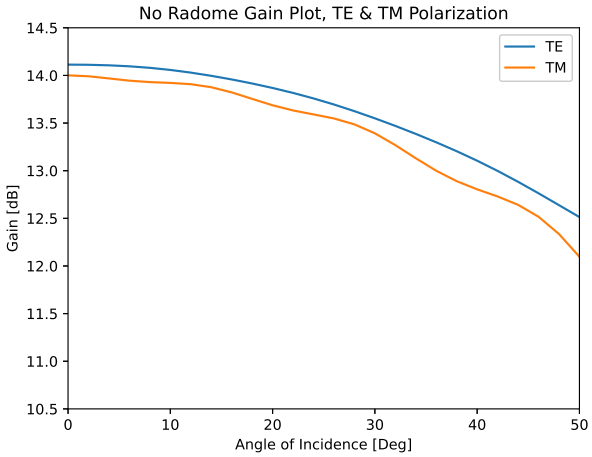

(a)

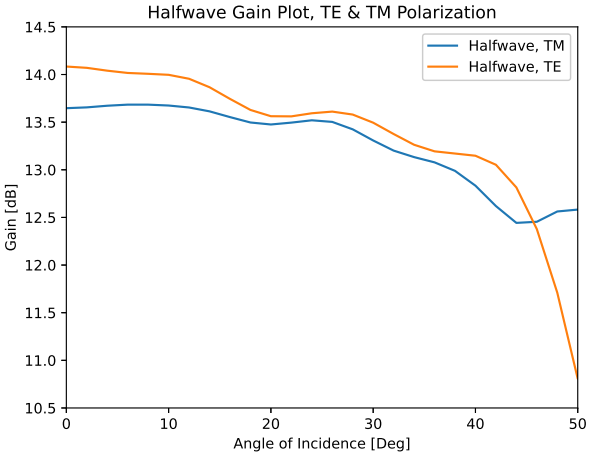

(b)

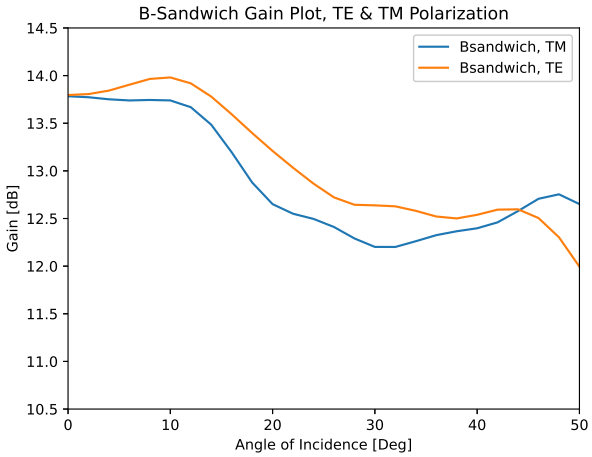

(c)

Figure 8.2: Maximum Gain for each angle of incidence. (a) shows the case for no radome, (b) is the half-wavelength and (c) shows the B-sandwich gain. Both polarizations are plotted in each case.

In figure 8.3, the gain difference between the case with and without a radome present is compared for both the half-wavelength and the B-sandwich radomes. Figure 8.3a shows the TE polarization case and figure 8.3b shows the TM-polarization case. We also included transmission simulations from HFSS for a flat radome for comparison.

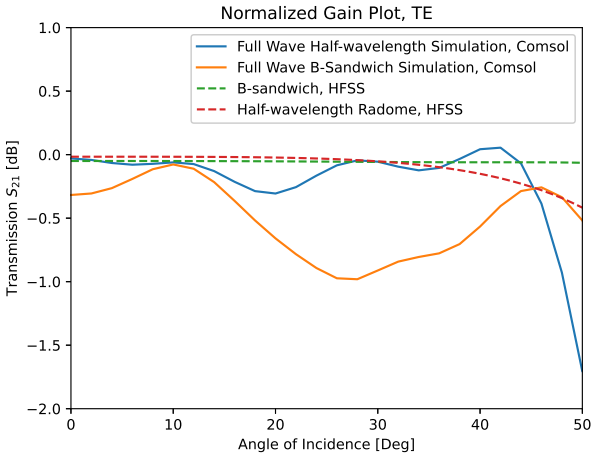

(a)

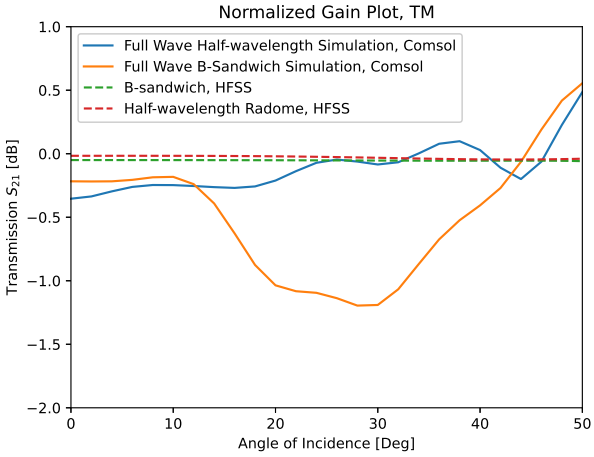

(b)

Figure 8.3: The normalized gain plots for the COMSOL Multiphysics simulations compared to the HFSS simulations. In (a) the TE polarization for the half-wavelength and B-sandwich respectively is shown. In (b) the TM polarization for both radomes are shown.

Another factor which can be investigated for the radome performance when analysing

antenna radiation is the bore-sight error (BSE). In figure 8.4 below the BSE for both polarizations for each radome is shown, the BSE here is the absolute difference between the angle of incidence and the bore-sight angle.

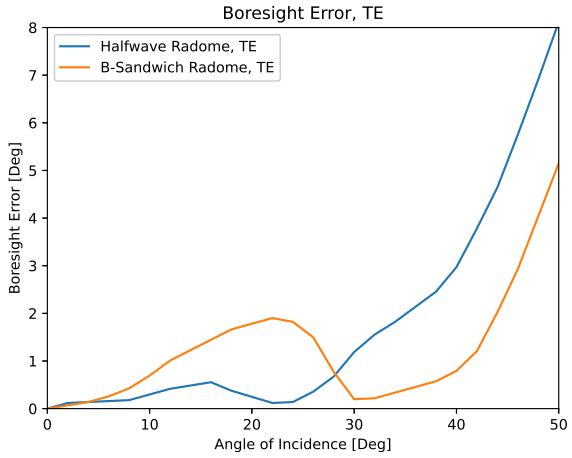

(a)

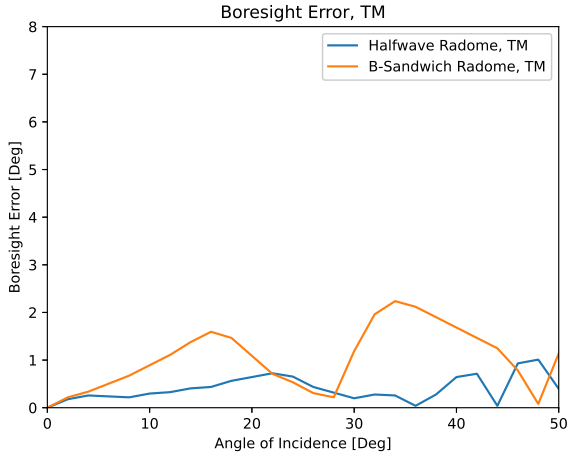

(b)

Figure 8.4: Boresight Error (BSE) plotted for each simulated radome. (a) shows the case for the TE polarization and (b) shows the TM polarization.

Chapter 9
Discussion

9.1 A-Sandwich

From the A-sandwich designs that we optimized and simulated we can see that our goal of having a reflectance below -25 dB for up to 50° degrees can be achieved; this can be seen in figure 6.5 and figure 6.7. With the A-sandwich design we also saw that it was only needed to optimize for the TE polarization as the performance of the TM polarization followed automatically. From the results it was noticed that for up to 50° degrees as seen in figure 6.5 the optimal design was with $N = 2$ cores.

If we compare the A-sandwich design optimized at normal incidence with the traditional half-wavelength radome as shown in figure 6.4, we see that in order to have better performance than the half-wavelength radome over a sweep for the angle of incidence we need exactly four cores; more cores are not necessarily preferable. The $N = 4$ sandwich is better since when we increase the number of cores we also increase the bandwidth of our radome [16]. The downside of this design is that with an increase in radome thickness we also introduce more losses which lowers the overall power reflection. This might explain why it is not advantageous to go over four cores, which means that there is a balance between increasing the bandwidth and avoid to many losses when increasing N

One important factor that we have not considered for the A-sandwich when analysing the results is the structural benefits of the A-sandwich. Depending on the use case an A-sandwich can be preferable due to the beneficial strength to weight ratio even if the electromagnetic performance might be slightly worse. Examples of this would be in for example aerospace engineering where A-sandwiches with honeycomb or porous material cores are used [36].

9.2 Honeycomb Simulations & Prototype Manufacturing

In figure 7.1 we can see the HFSS simulations of our honeycomb structures. What we see from this is that compared to the conventional solid core structure with the same relative dielectric constant we could design a honeycomb core with around a -10 dB decrease in performance at its maximum value.

Even if the performance of the honeycomb core is worse than that of the conventional we chose to produce this as the prototype due to our limitations. In the scope of our project it was not feasible to get a hold of low dielectric core materials such as Rohacell 71HF. Therefore, we chose to produce the honeycomb core which had a low relative dielectric constant and we could print the whole radome with one material. This is beneficial since we do not need to consider multiple materials as well as that we can tune the dielectric constant of the core. Possibly this can reduce the manufacturing cost.

One drawback when designing the honeycomb with our method is that in the Python optimizations using transmission line theory we cannot take the honeycomb structure itself into consideration, we can only optimize the solid core case. However, as we just saw in figure 7.1, the honeycomb is similar in performance to the conventional solid core case; especially if we reduce the honeycomb unit cell size in figure 3.3.

However, the reason why we chose a side-wall length of 3 mm is, as mentioned earlier, due to limitations of the printing process. The prototype was produced in PLA with a fused filament 3D-printer [48] which had limited resolution and the process was shown in chapter 7. The end-product came out well, there were slight structural errors due to the defect introduced in the printing process which made it such that the radome was not entirely flat. Also, the adhesive held well together and as seen in figure 7.3b the adhesive seems to not enter the honeycomb cavities.

An alternative that was discussed when producing the prototype was to print the whole radome as one piece. This is doable with filament printers but the threads will slightly bend into the honeycomb cavities. If the unit cell is larger then the thread will probably bend more. It is possible to produce this but since we have a relatively large unit cell we chose not to pursue this method.

9.3 Prototype Measurements

The assembly of the prototype came out well, however, there were slight structural errors due to one of the plates being bent during the printing process. The thickness of the adhesive has not been measured, however, we made an assumption that it was around 0.05 mm based on previous work in similar settings [49].

In figure 7.5 we can see the measurement results from the measured 3D-printed PLA half-wavelength radome. What we can see in the measurement and simulation of the half-wavelength radome is that the peak is slightly shifted from 24 GHz. This shift is likely due to that we initially designed the half-wavelength radome for a relative dielectric constant of 2.7 while the real value was 2.62; thus the thickness of the half-wavelength radome is not perfectly optimized at 24 GHz.

The measured honeycomb prototype is plotted in figure 7.6 together with the

simulated honeycomb. Here both have a relative dielectric constant of 2.6 which was the measured value. The overall behaviour of the transmission is somewhat close to that of the simulations; albeit shifted in frequency. But it is difficult to make final conclusions with these measurements because there could be several sources of error. We believe that the main differences in transmission between the prototype and the simulations arise from sources of error with the prototype as well as possible errors in the measurement setup. Our measurement set-up was far from optimal and a lot of noise and disturbances are introduced.

The first measurement that was performed in an open room had data that was unusable as there was too much noise from the environment in order to get a proper result. We solved this by moving our measurement set-up to a room covered in absorbing material, however, this does not eliminate the disturbances introduced due to our set-up itself. Further, since our sample was 20x20 cm^2 we could not have the horns at a too large distance which would give inaccurate results since the beam will illuminate the edges of the sample. What could be done in the future in order to make a more precise measurement is to use either a better set-up with proper alignment and a larger sample or measure via a wave-guide. Further, measurements with rotational tables can be performed in order to investigate oblique incidences and a prototype can also be produced which can be used for full radome measurements using a radar device.

Another source of error for our prototype is the additive manufacturing process. We had assumed beforehand that the PLA had a dielectric constant of 2.7 and when measured we got 2.62. The printing process itself gave some anomalies since one of the honeycomb plates was bent a bit, and from the results we could not identify if this affected the end result. Furthermore, the thickness of the adhesive and the relative dielectric constant had not been measured. These were assumed based on previous work [49], but could be both thicker or thinner.

9.4 B-Sandwich

It is interesting to see that some of the best optimized sandwiches has been the B-sandwich. A possible reason for the difference in performance between the A & B-sandwich comes from the dielectric constants of the material. In the B-sandwich we first have a gradually increasing dielectric constant in the layers going from the air to the core and then a decreasing dielectric constant when going the reverse direction from the core to air. With this design we get a more smooth transition between the dielectric layers which is preferred in order to maximize the performance [51]. The A-sandwich is the reverse case of the B-sandwich where we go from air to a much larger value of the dielectric constant and then to a low dielectric core, this then does not give a smooth transition which decreases the performance as compared to the B-sandwich [51].

A factor for why we chose to focus on the B-sandwich is that the aforementioned structural benefits of the A-sandwich are not relevant for our use case and thus

not considered. However, for a radome it is not desirable to have a soft (and potentially) water absorbing material as a skin. Neither is it desirable to have a honeycomb structure as the skin, since it will accumulate water and dirt and degrade the performance of the radome. With this we have a few limitations on the B-sandwich if we were to create a prototype or a design for production. Due to the mechanical restrictions with the B-type sandwich we realistically need a skin material that has sufficient mechanical resistance and at the same time has a low dielectric constant. Since the optimal performance of the B-type radome consists of an anti-reflective coating where $\epsilon_{\mathrm{r,skin}} = \sqrt{\epsilon_{\mathrm{r,core}}}$ we also have a limit on the $\epsilon_{\mathrm{r,skin}}$ since the it is difficult to have a dielectric constant for the core that is larger than 6.5. With these restrictions we see that our $\epsilon_{\mathrm{r,skin}}$ has the limits of $2 \leq \epsilon_{\mathrm{r,skin}} \leq 2.55$ [29].

As shown in (2.28), for zero degree angle of incidence, we would need that $\epsilon_{\mathrm{r,skin}} = \sqrt{\epsilon_{\mathrm{r,core}}}$ together with $d_{\mathrm{skin}} = (2n+1)\lambda/4$ to use the skin material as an anti-reflective coating [14]. In our case, however, we want not only to minimize reflection for $\theta = 0°$ but for a broad range of angles. As a rule of thumb however we have initially chosen to keep $\epsilon_{\mathrm{r,skin}} \approx \sqrt{\epsilon_{\mathrm{r,core}}}$ as this has shown to give good results, the downside of increasing values of the dielectric constant is that the bandwidth decrease slightly. It is also important to mention that the theoretical condition for an anti-reflective coating (2.28) assumes that there are no reflections after the second layer as it is assumed to be infinite.

The main difference we noticed when designing B-sandwiches as compared to the other designs was that when we only optimized for the TE polarization the TM polarization decreased in performance, as shown in figure 6.6. Due to this we changed our approach of optimization and considered both polarizations at the same time, which is shown in figure 6.9. Interestingly, from the results we noticed that for angles of incidence up to 50° degrees the $N = 2$ sandwich design gave the optimal performance, just as with the A-sandwich.

The final part we investigated with the B-sandwich was how the result would change if we optimized for different angles in the TE & TM case. The results can be seen in figure 6.10 and this gave very promising results. In figure 6.10a we have a minimum power reflection of -45 dB when optimizing up to 50° degrees for the TE case and up to 30° degrees for the TM case. This showed that we could increase the overall performance of the radome if the limitations in TE & TM are not the same.

Interestingly, in figure 6.10b we have the inverted case where the TM polarization was optimized for 50° degrees and TE optimized for 30° degrees instead. We do not know the exact reasons why this happens, but when looking in figure 6.11 we see that when solely optimizing for TE or TM respectively the B-sandwich optimized for TE is better than the B-sandwich optimized for TM. From this we reason that if TM polarization is optimized for a lower angle while TE is optimized at the same time for a larger angle there are more options for the TE which generally has a higher performance.

9.5 Finite Radome Simulations

COMSOL Multiphysics antenna simulations were performed in order to investigate the performance of, in this case, the half-wavelength radome and the B-sandwich radome. This was performed with a 2-dimensional COMSOL Multiphysics model for each polarization. In figure 8.2 the maximum gain for each angle in a parametric sweep between 0° and 50° is shown at exactly 24 GHz. We see, as expected, that the performance reduces when introducing a radome into the system.

In order to perform a meaningful analysis of the gain we have chosen to plot the gain difference for each radome at TE & TM polarization. This can be seen in figure 8.3. What we see here is that for both radomes we generally have a maximum difference of around -1 dB for both polarizations. The half-wavelength radome has better performance in general, however, we can see that for the higher angles of incidence the B-sandwich has a slight increase in performance as compared to the half-wavelength radome.

The results from the COMSOL Multiphysics gain plots are not entirely what was expected as compared to the simulations. In figure 8.3 this difference can be seen with the HFSS simulations as compared to the COMSOL Multiphysics simulations. However, the HFSS simulation does not include any parameters relating to the antenna and the radome geometry. That is to say, in COMSOL Multiphysics we have edges on the radome, sidewalls and reflections on the substrate. The difference in performance for the B-sandwich in the COMSOL Multiphysics simulations as compared to the HFSS and Python simulation most likely occur due to these factors. Also, the model itself will affect the simulation since the result is dependent on the dimensions of the radome as compared to that of the source. The inner height and length are the same for both the half-wavelength radome and the B-sandwich but the geometries of each radome might interact differently with the signal.

For antenna applications it is also of interest to investigate the boresight error that occurs due to the introduction of a radome. This is shown for the COMSOL Multiphysics simulations in figure 8.4 where 8.4a is the TE polarization and 8.4b is the TM polarization. From this we can see that the B-sandwich TE mode outperforms the half-wavelength radome at angles of incidence larger than 30° and for the TM mode the half-wavelength out performs the B-sandwich overall. What can also be seen from these results is that for the TM polarization is considerably less effected by the boresight error than the TE polarization.

9.6 Design Method

From what can be seen in the results is that the simulated radome structures that were developed with the help of Python algorithms, optimizations and HFSS simulations were shown to be close to that of the measured structures. With the produced honeycomb prototype we saw, as mentioned, that the results were similar to that of the simulations. This shows us that our method of design for the hon-

eycomb sandwich structures gives a valid result. This, combined with the results from the full simulation performed in COMSOL Multiphysics for the B-sandwich makes it such that we draw the conclusion that our design method is feasible for every sandwich radome structure. More work can be done in investigating multilayer structures, especially since from our results we can see that the tolerances are quite slim when introducing several layers all with different materials.

Also, one important part with our design is that since we focus on the goal of a reflectance of -25 dB or below, we do not take the transmittance into consideration. With a lossless material we have the condition of $R + T = 1$ [24] where R is the reflectance and T the transmittance. With this condition the transmittance which correlates to our goal of -25 dB should be larger than -0.014 dB. However, in reality we have losses in the materials which explains why the measured transmittance is lower than that of the lossless case. One could argue that a better method would have been to focus on the transmittance from the beginning. However, if the radome is optimized with respect to reflectance, then a well designed structure is found anyway. This is because transmittance is mostly affected by material choices rather than structural parameters.

9.7 Future Work

Much work can be done with improving on the results that we have achieved. Firstly, we had limitation in both time and production on our honeycomb prototype. With an alternative additive manufacturing method, or a more classical production approach, the size of our unit-cells (figure 3.3) can be made much smaller. This would make effective dielectric constant of the honeycomb layer more close to the Maxwell-Garnett approximation (3.4) [39], which would make the optimization in Python as well as the simulation more true to reality. Future projects could investigate the improvements within additive manufacturing, such as using a different technique than fused filament [48] as well as which alternative materials are available.

One part that can be investigated further is a prototype of the B-sandwich design which gave the optimal result from our optimizations. It is possible to create a prototype for this, although the manufacturing should be of very high quality since we have fairly low tolerances. It could also be interesting to see if it is possible to create a multi-layer prototype based on an optimization like the one in figure 6.13. Creating a prototype with several layers which requires very precise values on the dielectric constant as well as the layer thickness can be quite challenging due to the tolerances, especially if we have higher dielectric materials. The techniques we have used can also be combined, such as using honeycomb cores in a multi-layered stacked structure in order to create a specific dielectric constant.

One area of interest, but not a focus in this work, is frequency selective surfaces (FSS) and in some parts meta structures. There has been a lot of work done previously with for example FSS which can be used to alter the electromagnetic

properties of the structure, the FSS can for example be used as a filter which only transmits at specific frequencies [52, 53]. FSS can be incorporated into our radome design in order to for example reduce the reflections at certain angles [54] or reduce incoming noise from other signals.

Within this project we have chosen to only focus on a flat radome design, this since we are designing for an arbitrary antenna array and the performance will be the same independent on where the antenna is positioned. Further work can be done within this field by investigating different designs of the radome for specific applications. With our optimizations we can only take the flat radome case into consideration. Therefore future work could investigate possibilities to find easy implementable methods to optimize radomes of different shapes as well.

Chapter 10
Conclusion

In this thesis a design method for optimizing, producing and measuring a radome prototype was shown. With our design method a high performing radome, with the goal of having less than -25 dB up to an angle of incidence of 50° could be achieved. Additionally, it was shown that for the prototype an A-sandwich with a porous honeycomb core could be produced with additive manufacturing where the effective dielectric constant of the honeycomb core could be tuned. Additionally, it was shown that the optimal performance was given by the B-sandwich design where high structural integrity could be achieved with a high performance over the span of angles of incidence up to 50°. Interestingly, for the B-sandwich case the TE and TM polarizations had to be optimized simultaneously as we saw a decrease in TM performance when only optimizing for TE. The results of the honeycomb prototype could be improved with a more advanced additive manufacturing technique with higher resolution. It was shown that our measured prototype gave reasonable results but due to the manufacturing process this would need further investigation. For the full simulations in COMSOL Multiphysics, it can be seen that our method for a sandwich radome does not necessarily give a better result than the half-wavelength radome. But we have to take into consideration that if we change the dimensions and shape of the radome to another than the one we used in COMSOL Multiphysics then we also change the result, where the optimized B-sandwich could potentially give a better result than the half-wavelength slab. Nevertheless, we believe that using our optimization method is a good first path for choosing parameters and understanding which radome type can work well.

Bibliography

[1] Ilavarasu Sivagnanam et al. "An approach to the design of composite radome for airborne surveillance application". In: *International Journal of Mechanical Engineering and Technology* 9 (Feb. 2018), pp. 36–48.

[2] Merrill I. Skolnik. *radar - History of radar*. Jan. 2022. URL: https://www.britannica.com/technology/radar/History-of-radar (visited on 05/20/2022).

[3] Cyril Domb. *James Clerk Maxwell, Biography & Facts*. Apr. 2022. URL: https://www.britannica.com/biography/James-Clerk-Maxwell (visited on 05/20/2022).

[4] C.H Huelsmeyer. *Hertzian-wave Projecting and Receiving Apparatus Adapted to Indicate or Give Warning of the Presence of a Metallic Body, such as a Ship or a Train, in the Line of Projection of such Waves*. 1904. URL: https://worldwide.espacenet.com/patent/search/family/032164344/publication/GB190413170A?q=pn%3DGB190413170A.

[5] C.H Huelsmeyer. *Télémobiloscope*. 1904. URL: https://worldwide.espacenet.com/patent/search/family/001346919/publication/FR3793E?q=pn%3DFR3793E.

[6] Dave Tahmoush, Jerry Silvious, and Bob Bender. "Radar surveillance in urban environments". In: *2012 IEEE Radar Conference*. 2012, pp. 0220–0225. DOI: 10.1109/RADAR.2012.6212140.

[7] STMicroelectronics. *Automotive Radar*. URL: https://www.st.com/en/applications/adas/automotive-radar.html (visited on 05/20/2022).

[8] Liu Kaiyi et al. “Design of a New Generation of Weather Radar Intelligent Temperature and Humidity Monitoring System Based on ZigBee”. In: *2019 International Conference on Meteorology Observations (ICMO)*. 2019, pp. 1–3. DOI: 10.1109/ICMO49322.2019.9025847.

[9] Acconeer. *Acconeer EXPLORE THE NEXT SENSE*. URL: https://www.acconeer.com/ (visited on 05/20/2022).

[10] Dennis J. Kozakoff. *Analysis of radome-enclosed antennas*. Artech House, 2010. ISBN: 9781596934412.

[11] *The Birth of Radar and World War Two*. Mar. 2021. URL: https://www.radarmuseum.co.uk/history/world-war-two/ (visited on 05/20/2022).

[12] Erwin Kreyszig. *Advanced Engineering Mathematics, 8th Edition*. 8th. John Wiley & Sons, 1998.

[13] V. DiCaudo. “Determining optimum C-sandwich radome thicknesses by means of smith chart”. In: *IEEE Transactions on Antennas and Propagation* 15.6 (1967), pp. 821–822. DOI: 10.1109/TAP.1967.1139046.

[14] S.J. Orfanidis. *Electromagnetic Waves and Antennas*. Sophocles J. Orfanidis, 2016. URL: https://books.google.se/books?id=4n5ezQEACAAJ.

[15] Zeeshan Qamar, Nafati Aboserwal, and Jorge L. Salazar-Cerreno. “An Accurate Method for Designing, Characterizing, and Testing a Multi-Layer Radome for mm-Wave Applications”. In: *IEEE Access* 8 (2020), pp. 23041–23053. DOI: 10.1109/ACCESS.2020.2970544.

[16] Zeeshan Qamar, Jorge L. Salazar-Cerreno, and Nafati Aboserwal. “An Ultra-Wide Band Radome for High-Performance and Dual-Polarized Radar and Communication Systems”. In: *IEEE Access* 8 (2020), pp. 199369–199381. DOI: 10.1109/ACCESS.2020.3032881.

[17] Farhad Mazlumi. “Analysis and design of flat asymmetrical a-sandwich radomes”. In: *Journal of Telecommunication, Electronic and Computer Engineering* 10 (July 2018), pp. 9–13.

[18] *wave | Behavior, Definition, & Types*. Dec. 2016. URL: https://www.britannica.com/science/wave-physics (visited on 05/20/2022).

[19] National Aeronautics and Space Administartion, Science Mission Directorate. *Anatomy of an Electromagnetic Wave*. 2010. URL: https://science.nasa.gov/ems/02_anatomy (visited on 05/20/2022).

[20] Hubregt Visser. *Antenna Theory and Applications*. John Wiley & Sons, 2012. ISBN: 99781119944744.

[21] Raik Schnabel et al. “Reflection, Refraction, and Self-Jamming”. In: *IEEE Microwave Magazine* 13.3 (2012), pp. 107–117. DOI: 10.1109/MMM.2012.2186095.

[22] Greg Peake. Chethan Kumar. Habeeb Ur Rahman Mohammed. *mmWave Radar Radome Design Guide*. eng. Application Report. 2021.

[23] Pete Bevelacqua. *Antenna-Theory.com - Field Regions*. URL: https://www.antenna-theory.com/basics/fieldRegions.php (visited on 05/20/2022).

[24] Sundström et al. *Radio Electronics*. Electrical and Information Technology - Lund University, 2015.

[25] Fritz Caspers. “RF engineering basic concepts: S-parameters”. In: (Jan. 2012).

[26] Armin Parsa, Toshiro Kodera, and Christophe Caloz. “Ferrite Based Non-Reciprocal Radome, Generalized Scattering Matrix Analysis and Experimental Demonstration”. In: *IEEE Transactions on Antennas and Propagation* 59.3 (2011), pp. 810–817. DOI: 10.1109/TAP.2010.2103016.

[27] Toshiro Kodera, Armin Parsa, and Christophe Caloz. “Non-reciprocal ferrite antenna radome : The faradome”. In: *2009 IEEE Antennas and Propagation Society International Symposium*. 2009, pp. 1–4. DOI: 10.1109/APS.2009.5171697.

[28] Atefeh Mousavi. *Evaluation of radome effects on the radiation properties for a 24 GHz phased array antenna*. eng. Student Paper. 2020.

[29] Jan Barowski, Marc Zimmermanns, and Ilona Rolfes. “Millimeter-Wave Characterization of Dielectric Materials Using Calibrated FMCW Transceivers”. In: *IEEE Transactions on Microwave Theory and Techniques* 66.8 (2018), pp. 3683–3689. DOI: 10.1109/TMTT.2018.2854180.

[30] Johan Lundgren et al. “A Near-Field Measurement and Calibration Technique: Radio-Frequency Electromagnetic Field Exposure Assessment of Millimeter-Wave 5G Devices”. In: *IEEE Antennas and Propagation Magazine* 63.3 (2021), pp. 77–88. DOI: 10.1109/MAP.2020.2988517.

[31] E. Özi, A. V. Osipov, and T. F. Eibert. “Metamaterials for Microwave Radomes and the Concept of a Metaradome: Review of the Literature”. In: *International Journal of Antennas and Propagation* 2017 (2017), pp. 1–13. DOI: 10.1155/2017/1356108.

[32] Yuchu He and George V. Eleftheriades. "A Thin Double-Mesh Metamaterial Radome for Wide-Angle and Broadband Applications at Millimeter-Wave Frequencies". In: *IEEE Transactions on Antennas and Propagation* 68.3 (2020), pp. 2176–2185. DOI: 10.1109/TAP.2019.2951491.

[33] Zhao Pei et al. "Electromagnetic property of a novel gradient honeycomb composite fabricated by 3D forming". In: *Journal of Magnetism and Magnetic Materials* 493 (2020), p. 165742. ISSN: 0304-8853. DOI: https://doi.org/10.1016/j.jmmm.2019.165742. URL: https://www.sciencedirect.com/science/article/pii/S0304885319323480.

[34] Javad Shabanpour, Sina Beyraghi, and Homayoon Oraizi. "Reconfigurable honeycomb metamaterial absorber having incident angular stability". In: *Scientific Reports* 10.1 (2020). DOI: 10.1038/s41598-020-72105-4.

[35] Hsien-Ming Chang and Chungpin Liao. "A Parallel Derivation to the Maxwell-Garnett Formula for the Magnetic Permeability of Mixed Materials". In: *World Journal of Condensed Matter Physics* 01.02 (2011), pp. 55–58. DOI: 10.4236/wjcmp.2011.12009.

[36] Zhonggang Wang. "Recent advances in novel metallic honeycomb structure". In: *Composites Part B: Engineering* 166 (2019), pp. 731–741. ISSN: 1359-8368. DOI: https://doi.org/10.1016/j.compositesb.2019.02.011. URL: https://www.sciencedirect.com/science/article/pii/S1359836818328178.

[37] Reuven Shavit. "Sandwich Radomes". In: *Radome Electromagnetic Theory and Design*. 2018, pp. 15–38. DOI: 10.1002/9781119410850.ch2.

[38] Lie Liu et al. "Effective electromagnetic properties of honeycomb substrate coated with dielectric or magnetic layer". In: *Applied Physics A* 116 (Sept. 2014), pp. 901–905. DOI: 10.1007/s00339-014-8458-4.

[39] Arshad Karimbu Vallappil et al. "Metamaterial-Inspired Electrically Compact Triangular Antennas Loaded with CSRR and 3 x 3 Cross-Slots for 5G Indoor Distributed Antenna Systems". In: *Micromachines* 13.2 (2022). ISSN: 2072-666X. DOI: 10.3390/mi13020198. URL: https://www.mdpi.com/2072-666X/13/2/198.

[40] Anyong Qing. "Basics of Differential Evolution". In: *Differential Evolution in Electromagnetics*. Ed. by Anyong Qing and Ching Kwang Lee. Berlin, Heidelberg: Springer Berlin Heidelberg, 2010, pp. 19–42.

ISBN: 978-3-642-12869-1. DOI: 10.1007/978-3-642-12869-1_2. URL: https://doi.org/10.1007/978-3-642-12869-1_2.

[41] Rainer Storn and Kenneth Price. "Differential Evolution A Simple and Efficient Heuristic for global Optimization over Continuous Spaces". In: *Journal of Global Optimization* 11.4 (1997). DOI: 10.1023/a:1008202821328.

[42] Xin-She Yang. "Chapter 6 - Differential Evolution". In: *Nature-Inspired Optimization Algorithms*. Ed. by Xin-She Yang. Oxford: Elsevier, 2014, pp. 89–97. ISBN: 978-0-12-416743-8. DOI: https://doi.org/10.1016/B978-0-12-416743-8.00006-3. URL: https://www.sciencedirect.com/science/article/pii/B9780124167438000063.

[43] Jason Brownlee. *Differential Evolution Global Optimization With Python*. Oct. 2021. URL: https://machinelearningmastery.com/differential-evolution-from-scratch-in-python/ (visited on 05/20/2022).

[44] *scipy.optimize.differential_evolution SciPy v1.8.0 Manual*. URL: https://docs.scipy.org/doc/scipy/reference/generated/scipy.optimize.differential_evolution.html (visited on 05/20/2022).

[45] Karan Kumar Pradhan and Snehashish Chakraverty. "Chapter Four - Finite Element Method". In: (2019). Ed. by Karan Kumar Pradhan and Snehashish Chakraverty, pp. 25–28. DOI: https://doi.org/10.1016/B978-0-12-815492-2.00010-1. URL: https://www.sciencedirect.com/science/article/pii/B9780128154922000101.

[46] Marisa Melchiorre. *The Fundamentals of FEA Meshing for Structural Analysis*. Apr. 2022. URL: https://www.ansys.com/blog/fundamentals-of-fea-meshing-for-structural-analysis (visited on 05/20/2022).

[47] Qingkai Kong, Timmy Siauw, and Alexandre M. Bayen. "Chapter 23 - Boundary-Value Problems for Ordinary Differential Equations (ODEs)". In: *Python Programming and Numerical Methods*. Ed. by Qingkai Kong, Timmy Siauw, and Alexandre M. Bayen. Academic Press, 2021, pp. 399–414. ISBN: 978-0-12-819549-9. DOI: https://doi.org/10.1016/B978-0-12-819549-9.00033-6. URL: https://www.sciencedirect.com/science/article/pii/B9780128195499000336.

[48] Herb Weiner. *Fused Filament Fabrication Simply Explained*. Jan. 2020. URL: https://all3dp.com/2/fused-filament-fabrication-fff-3d-printing-simply-explained/.

[49] Johan Lundgren, Andreas Ericsson, and Daniel Sjöberg. “Design, Optimization and Verification of a Dual Band Circular Polarization Selective Structure”. In: *IEEE Transactions on Antennas and Propagation* 66.11 (2018), pp. 6023–6032. DOI: 10.1109/TAP.2018.2864540.

[50] Joel Dunsmore. “Gating effects in time domain transforms”. In: (Dec. 2008). DOI: 10.1109/ARFTG.2008.4804303.

[51] F Fitzek, R. Rasshofer, and E. Biebl. “Comparison of matching layers for automotive radome design”. In: *Advances in Radio Science* 8 (Sept. 2010), pp. 49–54. DOI: 10.5194/ars-8-49-2010.

[52] S. Celozzi, R. Araneo, and Giampiero Lovat. “Frequency Selective Surfaces”. In: Mar. 2008, pp. 219–240. ISBN: 9780470055366. DOI: 10.1002/9780470268483.ch10.

[53] C. Topcuoglu, C.D. Erbas, and N.T. Tokan. “Design and Implementation of Frequency Selective Radome for X-Band Applications.” In: *ACES* 34.10 (2019), pp. 1561–1567.

[54] Tao Ma et al. “A FSS with stable performance under large incident angles”. In: *Progress In Electromagnetics Research Letters* 41 (Jan. 2013), pp. 159–166. DOI: 10.2528/PIERL13061703.

Printed by Tryckeriet i E-huset, Lund 2022

LUND
UNIVERSITY

Series of Master's theses
Department of Electrical and Information Technology
LU/LTH-EIT 2022-866
http://www.eit.lth.se